

## EDGE ARTICLE

[View Article Online](#)  
[View Journal](#) | [View Issue](#)



Cite this: *Chem. Sci.*, 2020, **11**, 10669

All publication charges for this article have been paid for by the Royal Society of Chemistry

## Deciphering the origin of million-fold reactivity observed for the open core diiron $[\text{HO}-\text{Fe}^{\text{III}}-\text{O}-\text{Fe}^{\text{IV}}=\text{O}]^{2+}$ species towards C–H bond activation: role of spin-states, spin-coupling, and spin-cooperation<sup>†</sup>

Mursaleem Ansari,<sup>a</sup> Dhurairajan Senthilnathan<sup>\*b</sup> and Gopalan Rajaraman  <sup>\*a</sup>

High-valent metal–oxo species have been characterised as key intermediates in both heme and non-heme enzymes that are found to perform efficient aliphatic hydroxylation, epoxidation, halogenation, and dehydrogenation reactions. Several biomimetic model complexes have been synthesised over the years to mimic both the structure and function of metalloenzymes. The diamond-core  $[\text{Fe}_2(\mu-\text{O})_2]$  is one of the celebrated models in this context as this has been proposed as the catalytically active species in soluble methane monooxygenase enzymes (sMMO), which perform the challenging chemical conversion of methane to methanol at ease. In this context, a report of open core  $[\text{HO}(\text{L})\text{Fe}^{\text{III}}-\text{O}-\text{Fe}^{\text{IV}}(\text{O})(\text{L})]^{2+}$  (1) gains attention as this activates C–H bonds a million-fold faster compared to the diamond-core structure and has the dual catalytic ability to perform hydroxylation as well as desaturation with organic substrates. In this study, we have employed density functional methods to probe the origin of the very high reactivity observed for this complex and also to shed light on how this complex performs efficient hydroxylation and desaturation of alkanes. By modelling fifteen possible spin-states for 1 that could potentially participate in the reaction mechanism, our calculations reveal a doublet ground state for 1 arising from antiferromagnetic coupling between the quartet  $\text{Fe}^{\text{IV}}$  centre and the sextet  $\text{Fe}^{\text{III}}$  centre, which regulates the reactivity of this species. The unusual stabilisation of the high-spin ground state for  $\text{Fe}^{\text{IV}}=\text{O}$  is due to the strong overlap of  $\text{Fe}^{\text{IV}}\sigma_{z^2}^*$  with the  $\text{Fe}^{\text{III}}\pi_{xz}^*$  orbital, reducing the antibonding interactions via spin-cooperation. The electronic structure features computed for 1 are consistent with experiments offering confidence in the methodology chosen. Further, we have probed various mechanistic pathways for the C–H bond activation as well as –OH rebound/desaturation of alkanes. An extremely small barrier height computed for the first hydrogen atom abstraction by the terminal  $\text{Fe}^{\text{IV}}=\text{O}$  unit was found to be responsible for the million-fold activation observed in the experiments. The barrier height computed for –OH rebound by the  $\text{Fe}^{\text{III}}-\text{OH}$  unit is also smaller suggesting a facile hydroxylation of organic substrates by 1. A strong spin-cooperation between the two iron centres also reduces the barrier for second hydrogen atom abstraction, thus making the desaturation pathway competitive. Both the spin-state as well as spin-coupling between the two metal centres play a crucial role in dictating the reactivity for species 1. By exploring various mechanistic pathways, our study unveils the fact that the bridged  $\mu$ -oxo group is a poor electrophile for both C–H activation as well for –OH rebound. As more and more evidence is gathered in recent years for the open core geometry of sMMO enzymes, the idea of enhancing the reactivity via an open-core motif has far-reaching consequences.

Received 8th May 2020  
Accepted 16th June 2020

DOI: 10.1039/d0sc02624g  
[rsc.li/chemical-science](http://rsc.li/chemical-science)

## Introduction

High-valent metal–oxo complexes are of great interest due to their potent catalytic abilities.<sup>1–25</sup> Dinuclear metal–oxo complexes have different types of metal centres, but iron is the most common metal centre to oxidise C–H bonds through the dioxygen activation mechanism, in which high-valent oxo–iron species are often postulated and demonstrated to act as the actual oxidising species.<sup>26–33</sup> Membrane-bound methane

<sup>a</sup>Department of Chemistry, Indian Institute of Technology Bombay, Mumbai 400076, India. E-mail: [rajaraman@chem.iitb.ac.in](mailto:rajaraman@chem.iitb.ac.in)

<sup>b</sup>Center for Computational Chemistry, CRD, PRIST University, Vallam, Thanjavur, Tamilnadu 613403, India

† Electronic supplementary information (ESI) available. See DOI: [10.1039/d0sc02624g](https://doi.org/10.1039/d0sc02624g)



monooxygenases (MMOs) containing copper are known,<sup>34–37</sup> but the longest known MMOs are soluble proteins containing a dinuclear iron active site.<sup>27,38–40</sup> The high-valent intermediate Q of soluble methane monooxygenase (sMMO) is a two-electron oxidant that effects the hydroxylation of methane.<sup>41–47</sup> For these reasons, complexes based on high-valent iron have been proved to be a compelling tool in the activation of inert C–H bonds, both in biochemical and synthetic oxidation processes.<sup>48–50</sup>

The active site structure of the sMMO possesses an  $[\text{Fe}_2^{\text{IV}}(\mu\text{-O})]$  diamond core motif,<sup>45,51–56</sup> and this unit is known to be responsible for the activation of inert C–H bonds such as those of methane.<sup>57</sup> This has inspired several groups to utilise both heme<sup>50,58–60</sup> and non-heme<sup>61</sup> ligand frameworks to synthesise biomimetic models, which are both structural and functional mimics of the enzyme.<sup>62</sup> Among various reported diiron enzymes that possess diiron(IV) at the active centre, two classes of enzymes clearly emerge with enzymes such as sMMO or ToMO performing hydroxylation of aliphatic and aromatic substrates while enzymes such as  $\Delta 9$  desaturase ( $\Delta 9\text{D}$ )<sup>63–65</sup> perform desaturation of alkanes. The first step for both reactions is common. *i.e.* C–H bond activation while the second step involves competitive rebound of the –OH group (recombination) *vs.* activation of the second C–H bond (elimination) leading to an alkene as shown in Scheme 1.<sup>66</sup> There is also another class of diiron enzymes which catalyse the conversion of nucleotides to deoxynucleotides and among several classes, class Ia ribonucleotide reductases (RNR) are relevant to mention here as they employ  $\mu\text{-oxo-Fe}_2^{\text{III/IV}}$  to activate the C–H bond with very high selectivity.<sup>26</sup>

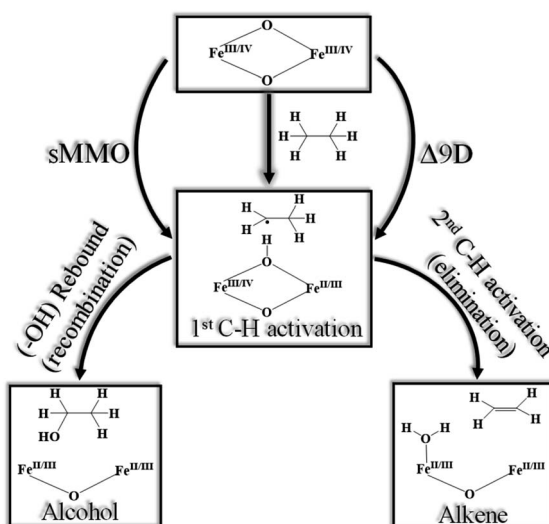
Various biomimetic dinuclear iron(IV) models were synthesised, and their reactivity were tested to understand their mechanistic features. Depending on the nature of ligands/bridging groups, there are two classes of dinuclear iron–oxo catalysts with some catalysts performing efficient hydroxylation and others desaturation. Examples of these catalysts include (i)

$[\text{Fe}_2^{\text{IV}}(\mu\text{-O})(\text{TAML})]^{2+}$  species reported by Collins and co-workers, which perform efficient hydroxylation of the benzylic substrate.<sup>12</sup> (ii)  $[\text{Fe}_2^{\text{IV}}(\mu\text{-O})_2(\text{TPA})_2]^{4+}$  reported by Xue *et al.*, which is a dinuclear iron complex that efficiently performs desaturation with 9,10-dihydroanthracene (DHA) to produce naphthalene.<sup>10,67,68</sup> (iii)  $[\text{Fe}_2^{\text{IV}}(\mu\text{-O})_2\text{L}]^{4+}$  (where L = *N,N*-bis-(3',5'-dimethyl-4'-methoxypyridyl-2'-methyl)-*N'*-acetyl-1,2-diaminoethane) reported by Que and co-workers, which also performs desaturation to yield cyclohexene from cyclohexane.<sup>69</sup> (iv) N-bridged high-valent heme diiron–oxo species reported by Sorokin and co-workers, which can activate alkanes such as methane and perform efficient hydroxylation.<sup>70–72</sup> In light of these results, a report by Xue *et al.* on  $[\text{X-Fe}^{\text{III}}\text{-O-Fe}^{\text{IV}}=\text{O}]^{2+}$  dinuclear unit gains attention as this complex is found to perform C–H activation nearly million-fold faster than other known complexes, and can perform both hydroxylation and desaturation depending on the nature of the substrate.<sup>67</sup> The nature of the active complex species in this reaction was unambiguously established earlier by Münck and co-workers using a bunch of spectroscopic tools (Mössbauer, EPR, and UV-visible).<sup>73,74</sup>

Theoretical studies play an important role in this area to obtain insight into the electronic structure of catalytically active species, and also to probe the mechanism of catalytic transformations.<sup>59,75</sup> There are numerous reports in the literature on the electronic structure and mechanistic studies of mononuclear high-valent iron–oxo species, but there are only limited studies on dinuclear iron–oxo species.<sup>71,72,76,77</sup> This is essentially due to the presence of numerous spin states arising from the exchange coupling between the two metal centres, and these states are often challenging to compute.<sup>57</sup> In this work, we aim to discuss the electronic structure of dinuclear iron oxidants to rationalise the extremely high reactivity that is observed for the  $[\text{HO(L)Fe}^{\text{III}}\text{-O-Fe}^{\text{IV}}(\text{O})(\text{L})]^{2+}$  (where L is tris(pyridine-2-yl)methyl amine) open core complex with the cyclopentane (CP) substrate using density functional theory (DFT). By studying the mechanistic features, we aim to answer the following intriguing questions which remain open in this area for a long time (i) what is the origin of million-fold reactivity towards C–H bond cleavage observed for this open core diiron–oxo species? (ii) Is a terminal  $\text{Fe}^{\text{IV}}=\text{O}$  more reactive than a bridged one? if so why? (iii) While most of the mono and dinuclear iron–oxo species perform selective hydroxylation or desaturation, this complex was found to perform both at ease, why? (iv) How important is the spin-state in controlling the reactivity in dinuclear systems? (v) The two iron centres are coupled *via* strong exchange interaction, is this strong-coupling offers an electronic/spin-cooperativity enabling higher/diverse reactivity?

## Computational details

All calculations reported were performed using the Gaussian 09 suite of programs.<sup>78</sup> By analysing these results along with all the previous observations, here we have chosen the B3LYP-D3 (ref. 79) functional for our study. The LACVP basis set comprising the LanL2DZ – Los Alamos effective core potential for Fe (ref. 80–82) and a 6-31G\*<sup>83</sup> basis set for the other atoms (carbon, nitrogen, oxygen, hydrogen, and chlorine) (B-I) were employed



Scheme 1 Generic mechanism for hydroxylation vs. desaturation by using sMMO (soluble methane monooxygenase)<sup>43</sup> and  $\Delta 9\text{D}$  (stearoyl-ACP  $\Delta^9$ -desaturase).<sup>63</sup>



for geometry optimisation and frequency calculations. Single point calculations were performed using a def2-TZVP<sup>84,85</sup> basis set (B-II) on the optimised geometries. The solvation energies were computed using the PCM solvation model,<sup>86</sup> where acetonitrile was used as a solvent. The fragment approach available in the Gaussian 09 program has been employed to obtain open-shell singlet states<sup>87</sup> and also to converge difficult multiplets. All the reported energies are B3LYP-D3 solvation energy (at the BS-II level) incorporating zero-point energy corrections (at the BS-I level) at 298.15 K. Additionally, for comparison, we have also given free-energy corrected energy values in the ESI (see Table S4a-c for C–H activation in the ESI).<sup>†</sup> To account for the effect of polarisation, the whole computations have been repeated (see Scheme 2) by adding two per-chlorite counter ions *i.e.*  $[\text{HO}(\text{L})\text{Fe}^{\text{III}}\text{O}\text{--}\text{Fe}^{\text{IV}}(\text{O})(\text{L})]^{2+}2[\text{OClO}_3]^-$ . The transition states were characterised by a single imaginary frequency which pertains to the desired motion as visualised in Chemcraft<sup>88</sup> and Molden.<sup>89</sup> The choice of functional for this study is based on our as well as other groups' reports on diiron(IV)–oxo complexes.<sup>67,77,90–94</sup> Also, de Visser *et al.*<sup>72</sup> tested a series of functionals (B3LYP, B3LYP\*, BP86, M06-L, and PBE0) on  $\mu$ -nitrido–diiron(IV)–oxo species and supported the use of the B3LYP functional for the reproduction of structure, spin state patterns, and spectral parameters.<sup>72,95–100</sup> Furthermore, Chen *et al.* employed a similar methodology for their study on C–H/O–H/O–O bond activation using diiron(IV)–oxo species to gain insights into various mechanistic aspects and showed that this methodology can reproduce various experimental spectral parameters, offering confidence in the methodology chosen here.<sup>101–103</sup> In our calculations, we have

chosen cyclopentane as the substrate to test the hydroxylation *vs.* desaturation mechanism for simplicity, while experimentally tetrahydrofuran (THF), and other alkanes are used as the substrates. As both the substrates have similar C–H bond dissociation energy,<sup>104,105</sup> and earlier experimental and theoretical studies have been undertaken using cyclopentane, here we chose to study the mechanism with this substrate.

In diiron complexes, the magnetic exchange ( $J$ ) between both iron centres is computed by employing the following spin Hamiltonian,

$$\hat{H} = -JS_1 \cdot S_2$$

here, the negative  $J$  value corresponds to antiferromagnetic interaction, while a positive  $J$  value corresponds to ferromagnetic interaction. For calculating  $J$  values, the energies of the high spin state ( $E_{\text{HS}}$ ) and the low spin state ( $E_{\text{BS}}$ ) are computed using the broken symmetry (BS) approach developed by Noddeman.<sup>106–108</sup> Natural bond orbital (NBO), spin natural orbital (SNO), and MO analyses<sup>109</sup> were performed using G09 and visualisations were examined using Chemcraft software. Here, we have used notations for easy understanding of the various spin states, for instance,  $^{2S+1}[\text{species name}]_X$  where, S represents the spin state of the metal and X represents the spin configuration of the Fe atom where high spin is denoted as  $hs$ , intermediate spin as  $is$  and low spin as  $ls$ . We have utilized energy decomposition analysis (EDA)<sup>110,111</sup> to understand the origin of barrier heights.<sup>112–114</sup> This analysis is applied to H-atom abstraction step with the barrier height of ( $\Delta E^\ddagger$ ). This is defined as follows in eqn (1a):

$$\Delta E^\ddagger = \Delta E_{\text{def}} + \Delta E_{\text{int}} \quad (1a)$$

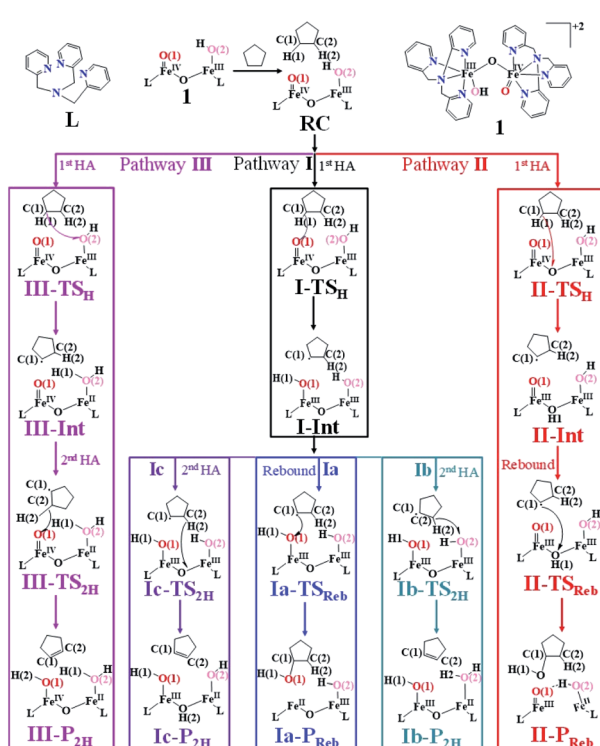
Where,

$$\Delta E_{\text{int}} = \Delta E_{\text{orb}} + \Delta E_{\text{el}} + \Delta E_{\text{Pauli(steric)}} \quad (1b)$$

The total deformation energy ( $\Delta E_{\text{def}}$ ) is defined as the energy required for distorting the substrate and the oxidant to their geometries in the transition state (TS). The  $\Delta E_{\text{int}}$  is the interaction energy, which is the energy between the deformed reactants as they are brought to their distances in the TS. The interaction energy (eqn (1b)) can be stabilising ( $\Delta E_{\text{int}} < 0$ ) due to the fact that the orbital mixing term ( $\Delta E_{\text{orb}}$ ) is dominant and there is a favourable electrostatic interaction ( $\Delta E_{\text{el}}$ ). Alternatively,  $\Delta E_{\text{int}}$  can be destabilising ( $\Delta E_{\text{int}} > 0$ ) because of steric repulsions (labelled in eqn (1b) as  $\Delta E_{\text{Pauli(steric)}}$ ).<sup>115</sup>

## Results and discussion

Que and co-workers reported a dinuclear  $[\text{HO}(\text{L})\text{Fe}^{\text{III}}\text{O}\text{--}\text{Fe}^{\text{IV}}(\text{O})(\text{L})]^{2+}$  (**1**) complex (where L is tris((4-methoxy-3,5-dimethylpyridin-2-yl)methyl)amine) and thoroughly characterized the same using several spectroscopic techniques. Anisotropic EPR signals at  $g = 2.00$ , which broaden when  $^{57}\text{Fe}$  containing nuclear spins are introduced, reveal that the ground state spin for this molecule is  $S = 1/2$  and the signals originate from iron centres and are not radical based. Mössbauer spectra



Scheme 2 The schematic mechanism of oxidation of cyclopentane by complex **1**  $[\text{HO}(\text{L})\text{Fe}^{\text{III}}\text{O}\text{--}\text{Fe}^{\text{IV}}(\text{O})(\text{L})]^{2+}$ .

reveal strong antiferromagnetic coupling between two Fe centres with the Fe<sup>III</sup> site ( $S_a$ ) being in the high-spin state ( $S_a = 5/2$ ) and the Fe<sup>IV</sup> site being in the high-spin quintet state ( $S_b = 2$ ) leading to a ground spin state  $S_T = 1/2$ .<sup>8</sup> Species **1** is found to be an aggressive oxidant towards a variety of substrates and the measured kinetics reveal that its reactivity is as good as that of taurine:  $\alpha$ -ketoglutarate dioxygenase (TauD) as well as a shape-selective catalyst [Fe(Tp<sup>Ph2</sup>)OBz] (where Tp<sup>Ph2</sup> = hydrotris(3,5-diphenylpyrazol-1-yl)borate and OBz = benzoate) – a rare feat to achieve in biomimetic chemistry.<sup>66</sup> Particularly, species **1** is found to perform the oxygen atom transfer reaction with diphenyl(pentafluorophenyl)phosphine and activate the C–H bonds of DHA to anthracene and convert even inert substrates such as tetrahydrofuran (THF) to  $\gamma$ -butyrolactone very efficiently. Particularly **1** is found to cleave the C–H bond nearly 100 to million-fold faster compared to several dinuclear Fe systems containing the diamond-core motif.<sup>8</sup> Further, the catalytic abilities of **1** are at least six times better compared to some of the strongest diiron(IV)-oxo species known.<sup>69</sup> Above all, its efficacy to perform C–H bond activation followed by elimination to

yield anthracene and with THF its ability to perform C–H bond activation followed by –OH rebound to yield tetrahydrofuran-2-ol (that eventually undergoes further oxidation to yield the observed  $\gamma$ -butyrolactone product) have puzzled us to look into its electronic structure and its catalytic abilities. This is rather a unique feat compared to other oxidants such as **1** due to both elimination and –OH rebound at ease, unlike other biomimetic models or enzymes which are generally selective towards desaturation or hydroxylation. In the forthcoming section, we first establish the electronic structure of **1**, and in the subsequent sections, its catalytic potential is explored.

### Electronic structure of $[\text{HO}(\text{L})\text{Fe}^{\text{III}}\text{--O--Fe}^{\text{IV}}(\text{O})(\text{L})]^{2+}$ (**1**)

The presence of two iron centres leads to the existence of various spin states, and strong coupling between the two centres results in a very complex spin state structure for **1**. For example, the Fe<sup>III</sup> centre can have spin  $S_a = 5/2, 3/2$ , and  $1/2$  while the Fe<sup>IV</sup> centre can have spin  $S_b = 2, 1$ , and  $0$  as their individual spin states. Further, the nature of the coupling between the two centres could be ferromagnetic or

Table 1 Different possible spin state electronic configurations of complex **1**

#### Electronic configuration

Spin state	Fe <sup>III</sup> ( $S_a$ )	Fe <sup>IV</sup> ( $S_b$ )	Relative energy (in $\text{kJ mol}^{-1}$ )	Coupling	Total spin $S_T$
<sup>10</sup> <b>1</b> <sub>(hs,hs)</sub>	$\uparrow$ $\delta_{xy}$ $\uparrow$ $\pi_{yz}^*$ $\uparrow$ $\pi_{xz}^*$ $\uparrow$ $\sigma_{x^2-y^2}^*$ $\uparrow$ $\sigma_{z^2}^*$	$\uparrow$ $\delta_{xy}$ $\uparrow$ $\pi_{yz}^*$ $\uparrow$ $\pi_{xz}^*$ $\uparrow$ $\sigma_{x^2-y^2}^*$ $\uparrow$ $\sigma_{z^2}^*$	15.6	F	9/2
<sup>2</sup> <b>1</b> <sub>(hs,hs)</sub>	$\uparrow$ $\delta_{xy}$ $\uparrow$ $\pi_{yz}^*$ $\uparrow$ $\pi_{xz}^*$ $\uparrow$ $\sigma_{x^2-y^2}^*$ $\uparrow$ $\sigma_{z^2}^*$	$\downarrow$ $\delta_{xy}$ $\downarrow$ $\pi_{yz}^*$ $\downarrow$ $\pi_{xz}^*$ $\downarrow$ $\sigma_{x^2-y^2}^*$ $\downarrow$ $\sigma_{z^2}^*$	0.0	AF	1/2
<sup>8</sup> <b>1</b> <sub>(hs,is)</sub>	$\uparrow$ $\delta_{xy}$ $\uparrow$ $\pi_{yz}^*$ $\uparrow$ $\pi_{xz}^*$ $\uparrow$ $\sigma_{x^2-y^2}^*$ $\uparrow$ $\sigma_{z^2}^*$	$\uparrow\downarrow$ $\delta_{xy}$ $\uparrow$ $\pi_{yz}^*$ $\uparrow$ $\pi_{xz}^*$ $\uparrow$ $\sigma_{x^2-y^2}^*$ $\uparrow$ $\sigma_{z^2}^*$	46.3	F	72
<sup>4</sup> <b>1</b> <sub>(hs,is)</sub>	$\uparrow$ $\delta_{xy}$ $\uparrow$ $\pi_{yz}^*$ $\uparrow$ $\pi_{xz}^*$ $\uparrow$ $\sigma_{x^2-y^2}^*$ $\uparrow$ $\sigma_{z^2}^*$	$\downarrow$ $\delta_{xy}$ $\uparrow$ $\pi_{yz}^*$ $\uparrow$ $\pi_{xz}^*$ $\uparrow$ $\sigma_{x^2-y^2}^*$ $\uparrow$ $\sigma_{z^2}^*$	48.4	AF	3/2
<sup>6</sup> <b>1</b> <sub>(hs,ls)</sub>	$\uparrow$ $\delta_{xy}$ $\uparrow$ $\pi_{yz}^*$ $\uparrow$ $\pi_{xz}^*$ $\uparrow$ $\sigma_{x^2-y^2}^*$ $\uparrow$ $\sigma_{z^2}^*$	$\uparrow\downarrow$ $\delta_{xy}$ $\uparrow$ $\pi_{yz}^*$ $\uparrow$ $\pi_{xz}^*$ $\uparrow$ $\sigma_{x^2-y^2}^*$ $\uparrow$ $\sigma_{z^2}^*$	67.3	—	5/2
<sup>8</sup> <b>1</b> <sub>(is,hs)</sub>	$\uparrow\downarrow$ $\delta_{xy}$ $\uparrow$ $\pi_{yz}^*$ $\uparrow$ $\pi_{xz}^*$ $\uparrow$ $\sigma_{x^2-y^2}^*$ $\uparrow$ $\sigma_{z^2}^*$	$\uparrow$ $\delta_{xy}$ $\uparrow$ $\pi_{yz}^*$ $\uparrow$ $\pi_{xz}^*$ $\uparrow$ $\sigma_{x^2-y^2}^*$ $\uparrow$ $\sigma_{z^2}^*$	37.8	F	7/2
<sup>2</sup> <b>1</b> <sub>(is,hs)</sub>	$\uparrow\downarrow$ $\delta_{xy}$ $\downarrow$ $\pi_{yz}^*$ $\uparrow$ $\pi_{xz}^*$ $\uparrow$ $\sigma_{x^2-y^2}^*$ $\uparrow$ $\sigma_{z^2}^*$	$\uparrow$ $\delta_{xy}$ $\uparrow$ $\pi_{yz}^*$ $\uparrow$ $\pi_{xz}^*$ $\uparrow$ $\sigma_{x^2-y^2}^*$ $\uparrow$ $\sigma_{z^2}^*$	32.6	AF	1/2
<sup>6</sup> <b>1</b> <sub>(is,is)</sub>	$\uparrow\downarrow$ $\delta_{xy}$ $\uparrow$ $\pi_{yz}^*$ $\uparrow$ $\pi_{xz}^*$ $\uparrow$ $\sigma_{x^2-y^2}^*$ $\uparrow$ $\sigma_{z^2}^*$	$\uparrow\downarrow$ $\delta_{xy}$ $\uparrow$ $\pi_{yz}^*$ $\uparrow$ $\pi_{xz}^*$ $\uparrow$ $\sigma_{x^2-y^2}^*$ $\uparrow$ $\sigma_{z^2}^*$	74.7	F	5/2
<sup>2</sup> <b>1</b> <sub>(is,is)</sub>	$\uparrow\downarrow$ $\delta_{xy}$ $\uparrow$ $\pi_{yz}^*$ $\uparrow$ $\pi_{xz}^*$ $\uparrow$ $\sigma_{x^2-y^2}^*$ $\uparrow$ $\sigma_{z^2}^*$	$\downarrow$ $\delta_{xy}$ $\uparrow$ $\pi_{yz}^*$ $\uparrow$ $\pi_{xz}^*$ $\uparrow$ $\sigma_{x^2-y^2}^*$ $\uparrow$ $\sigma_{z^2}^*$	73.0	AF	1/2
<sup>4</sup> <b>1</b> <sub>(is,ls)</sub>	$\uparrow\downarrow$ $\delta_{xy}$ $\uparrow$ $\pi_{yz}^*$ $\uparrow$ $\pi_{xz}^*$ $\uparrow$ $\sigma_{x^2-y^2}^*$ $\uparrow$ $\sigma_{z^2}^*$	$\uparrow\downarrow$ $\delta_{xy}$ $\uparrow$ $\pi_{yz}^*$ $\uparrow$ $\pi_{xz}^*$ $\uparrow$ $\sigma_{x^2-y^2}^*$ $\uparrow$ $\sigma_{z^2}^*$	112.4	—	3/2
<sup>6</sup> <b>1</b> <sub>(ls,hs)</sub>	$\uparrow\downarrow$ $\delta_{xy}$ $\uparrow$ $\pi_{yz}^*$ $\uparrow$ $\pi_{xz}^*$ $\uparrow$ $\sigma_{x^2-y^2}^*$ $\uparrow$ $\sigma_{z^2}^*$	$\uparrow$ $\delta_{xy}$ $\uparrow$ $\pi_{yz}^*$ $\uparrow$ $\pi_{xz}^*$ $\uparrow$ $\sigma_{x^2-y^2}^*$ $\uparrow$ $\sigma_{z^2}^*$	46.3	F	7/2
<sup>4</sup> <b>1</b> <sub>(ls,hs)</sub>	$\uparrow\downarrow$ $\delta_{xy}$ $\uparrow\downarrow$ $\pi_{yz}^*$ $\uparrow$ $\pi_{xz}^*$ $\uparrow$ $\sigma_{x^2-y^2}^*$ $\uparrow$ $\sigma_{z^2}^*$	$\uparrow$ $\delta_{xy}$ $\uparrow\downarrow$ $\pi_{yz}^*$ $\uparrow$ $\pi_{xz}^*$ $\uparrow$ $\sigma_{x^2-y^2}^*$ $\uparrow$ $\sigma_{z^2}^*$	80.8	AF	3/2
<sup>4</sup> <b>1</b> <sub>(ls,ls)</sub>	$\uparrow\downarrow$ $\delta_{xy}$ $\uparrow\downarrow$ $\pi_{yz}^*$ $\uparrow$ $\pi_{xz}^*$ $\uparrow$ $\sigma_{x^2-y^2}^*$ $\uparrow$ $\sigma_{z^2}^*$	$\uparrow\downarrow$ $\delta_{xy}$ $\uparrow\downarrow$ $\pi_{yz}^*$ $\uparrow$ $\pi_{xz}^*$ $\uparrow$ $\sigma_{x^2-y^2}^*$ $\uparrow$ $\sigma_{z^2}^*$	99.3	F	3/2
<sup>2</sup> <b>1</b> <sub>(ls,ls)</sub>	$\uparrow\downarrow$ $\delta_{xy}$ $\uparrow\downarrow$ $\pi_{yz}^*$ $\uparrow$ $\pi_{xz}^*$ $\uparrow$ $\sigma_{x^2-y^2}^*$ $\uparrow$ $\sigma_{z^2}^*$	$\uparrow\downarrow$ $\delta_{xy}$ $\uparrow\downarrow$ $\pi_{yz}^*$ $\uparrow$ $\pi_{xz}^*$ $\uparrow$ $\sigma_{x^2-y^2}^*$ $\uparrow$ $\sigma_{z^2}^*$	98.9	AF	1/2
<sup>2</sup> <b>1</b> <sub>(ls,ls)</sub>	$\uparrow\downarrow$ $\delta_{xy}$ $\uparrow\downarrow$ $\pi_{yz}^*$ $\uparrow$ $\pi_{xz}^*$ $\uparrow$ $\sigma_{x^2-y^2}^*$ $\uparrow$ $\sigma_{z^2}^*$	$\uparrow\downarrow$ $\delta_{xy}$ $\uparrow\downarrow$ $\pi_{yz}^*$ $\uparrow$ $\pi_{xz}^*$ $\uparrow$ $\sigma_{x^2-y^2}^*$ $\uparrow$ $\sigma_{z^2}^*$	136.6	—	1/2



antiferromagnetic leading to different total spin multiplicity. Due to the difference in the oxidation state and the ligand environment, it is possible that two Fe centres could exhibit different spin states from each other. These three scenarios lead to fifteen different spin states that are possible for **1**, and all these states are listed in Table 1. To understand the origin of the high-spin state observed for both the Fe<sup>III</sup> and Fe<sup>IV</sup> centres, we performed calculations on fictitious models of complex **1** where the individual Fe centres are replaced by diamagnetic analogs to get a grasp on the spin ladder of  $S_a$  and  $S_b$  (models are  $[\text{HO(L)}\text{Fe}^{\text{III}}-\text{O}-\text{Ti}^{\text{IV}}(\text{O})(\text{L})]^{2+}$ ,  $[\text{HO(L)}\text{Co}^{\text{III}}-\text{O}-\text{Fe}^{\text{IV}}(\text{O})(\text{L})]^{2+}$  and  $[\text{HO(L)}\text{Ga}^{\text{III}}-\text{O}-\text{Fe}^{\text{IV}}(\text{O})(\text{L})]^{2+}$ ; note here that all the substituted metal ions have the  $S = 0$  ground state).<sup>116</sup> These model studies reveal that the Fe<sup>III</sup> centre has the  $S_a = 5/2$  ground state with the  $S_a = 1/2$  first excited state lying at 43.6 kJ mol<sup>-1</sup> and the  $3/2$  state at 58.8 kJ mol<sup>-1</sup> from the ground state. For the Fe<sup>IV</sup> centre,  $S_b = 2$  is found to be the ground state for both Co<sup>III</sup> and Ga<sup>III</sup> ion substitutions with the  $S_b = 1$  first excited state being 55.2 and 41.3 kJ mol<sup>-1</sup> higher, respectively.

This reveals that independent of the spin-coupling, the Fe<sup>IV</sup> centre has a high-spin ground state. As  $S = 1$  is the ground state for the popular  $[\text{N}_4\text{PyFe}^{\text{IV}}=\text{O}]^{2+}$  species,<sup>117-127</sup> it is clear that replacing one of the nitrogen donors with an oxygen donor weakens the ligand field leading to the stabilisation of the unusual  $S = 2$  state (a reduction of 0.56 eV in the  $\Delta E(\text{d}_{xz} - \text{d}_{x^2-y^2})$  orbital gap, see Fig. S1 and S2 in the ESI†). Additionally, calculations performed on the mononuclear  $[\text{O(L)}\text{Fe}^{\text{IV}}-\text{OH}_2]^{2+}$  fictitious model derived from the dinuclear motif yield  $S = 1$  as the ground state with  $S = 2$  marginally higher in energy (5.6 kJ mol<sup>-1</sup>). This suggests that the second metal centre is important in stabilising the  $S = 2$  state at the Fe<sup>IV</sup>=O site.

To further probe the origin of the high-spin ground state, we have also carried out calculations on  $[\text{HO(L)}\text{Fe}^{\text{IV}}-\text{O}-\text{Fe}^{\text{IV}}(\text{O})(\text{L})]^{3+}$  models wherein both the Fe<sup>IV</sup> centres were found to have the  $S = 1$  ground state coupled ferromagnetically to each other leading to an overall  $S = 2$  state. Here the individual high-spin state of Fe<sup>IV</sup> is 35.8 kJ mol<sup>-1</sup> higher in energy compared to their corresponding triplet state revealing a fact that it is the +3 oxidation state of the neighbouring metal ion that weakens the ligand field leading to the stabilisation of the  $S = 2$  state (see Fig. S3 and Table S2 in the ESI†).<sup>128</sup> Among all the states computed, the  $^2\mathbf{1}_{\text{hs-hs}}$  doublet state is found to be the ground state and this is followed by  $^{10}\mathbf{1}_{\text{hs-hs}}$ ,  $^8\mathbf{1}_{\text{hs-is}}$ ,  $^4\mathbf{1}_{\text{hs-is}}$ ,  $^6\mathbf{1}_{\text{hs-ls}}$ ,  $^8\mathbf{1}_{\text{is-hs}}$ ,  $^2\mathbf{1}_{\text{is-hs}}$ ,  $^6\mathbf{1}_{\text{is-is}}$ ,  $^4\mathbf{1}_{\text{is-ls}}$ ,  $^6\mathbf{1}_{\text{ls-hs}}$ ,  $^4\mathbf{1}_{\text{ls-hs}}$ ,  $^4\mathbf{1}_{\text{ls-is}}$ ,  $^2\mathbf{1}_{\text{ls-is}}$ , and  $^2\mathbf{1}_{\text{ls-ls}}$  states in the order of increasing energy with an energy margin of 15.6, 46.3, 48.4, 67.6, 37.8, 32.6, 74.7, 73.0, 112.4, 46.3, 80.8, 99.3, 98.9 and 136.6 kJ mol<sup>-1</sup> respectively (see Table 1). Our energy calculations reveal that the Fe<sup>III</sup> ( $S_a$ ) and Fe<sup>IV</sup> ( $S_b$ ) centres possess a high spin state as their ground state, and these states are antiferromagnetically coupled leading to the  $S_T = 1/2$  ground state, and this is also consistent with the experiments.<sup>9,129</sup> This result is also consistent with other dinuclear  $\{\text{Fe}^{\text{III}}-\mu(\text{O})-\text{Fe}^{\text{IV}}\}$  reports where  $S_T = 1/2$  is found to be the ground state.<sup>8</sup> While traditionally DFT methods have been used to compute the energetics, recently several *ab initio* methods such as CASSCF/NEVPT2 and DLPNO-CCSD(T) are gaining attention in obtaining numerically superior results, although

they have their limitations in terms of active space/size of the models.<sup>118,127,130-138</sup> The optimised structure, and the spin density plot of the  $^2\mathbf{1}_{\text{hs-hs}}$  state are shown in Fig. 1a and b, where both the Fe centres are in a distorted octahedral geometry (see also Table S3 in the ESI†).<sup>139</sup> The 3d atomic orbitals of the iron atom of  $\text{Fe}^{\text{IV}}=\text{O}$  species form bonding and antibonding combinations with the oxygen atomic orbitals. Here the  $\delta$ -type  $\text{d}_{xy}$  orbital is found to be the lowest in energy followed by a degenerate pair of singly occupied  $\pi^*$  orbitals made from the antibonding combinations of the oxygen  $2\text{p}_x$  ( $2\text{p}_y$ ) with the iron  $3\text{d}_{xz}$  ( $3\text{d}_{yz}$ ) atomic orbitals. The singly occupied orbital of the  $\text{d}_{x^2-y^2}$  is antibonding in the in-plane Fe-N/ $\mu$ O linkage while one virtual  $\text{d}_z$  orbital has an antibonding character along the N1-Fe<sup>IV</sup>-O1 axis (see Fig. 1a and S2 in the ESI†). The Fe<sup>III</sup> and Fe<sup>IV</sup> high-spin states were found to have the electronic configurations of  $(\delta_{xy})^1 (\pi_{yz}^*)^1 (\pi_{xz}^*)^1 (\sigma_{x^2-y^2}^*)^1 (\sigma_{z^2}^*)^1$  and  $(\delta_{xy})^1 (\pi_{yz}^*)^1 (\pi_{xz}^*)^1 (\sigma_{x^2-y^2}^*)^1 (\sigma_{z^2}^*)^0$ , respectively, for the  $^2\mathbf{1}_{\text{hs-hs}}$  state (see also Fig. S2† for  $^2\mathbf{1}_{\text{hs-hs}}$  and Fig. S4 in the ESI† for other spin states).

In  $^2\mathbf{1}_{\text{hs-hs}}$ , the hydroxo group in the Fe<sup>III</sup> centre and oxo group in the Fe<sup>IV</sup> centre have strong H-bonding interaction ( $\text{O}(1)-\text{H} = 1.856$  Å), and this significantly reduces the  $\angle \text{Fe}^{\text{IV}}-\mu\text{O}-\text{Fe}^{\text{III}}$  angle to  $123^\circ$  compared to  $154^\circ$  known for other unsupported diiron species.<sup>12</sup> Additionally, the *trans*-N-Fe<sup>IV</sup>=O bond angle is found to be  $169^\circ$ , and this bent significantly compared to most of the mononuclear Fe<sup>IV</sup>=O species and has been attributed to higher reactivity in  $[\text{N}_2\text{Py}2\text{QFe}^{\text{IV}}=\text{O}]^{2+}$  species. This ferryl-bent that has also been witnessed in the reported X-ray structure<sup>140</sup> suggests that the bending can also lower the energy of the Fe<sup>IV</sup>  $\sigma_{z^2}^*$  orbital. Here the ferryl-bent observed is more severe than the reported complex due to the presence of the additional metal centre, strong H-bonding interaction between the Fe<sup>IV</sup>=O unit and the -OH group of the Fe<sup>III</sup> centre and the C-H $\cdots$ O interactions between the ferryl-oxygen and the hydrogen atom of the pyridine rings.<sup>140,141</sup> The earlier spectroscopic and theoretical study also confirms that the angle is very acute for this species, and the estimated angle is consistent with the value obtained from EXAFS measurements.<sup>8,73</sup> The Fe- $\mu$ O bond distances are found to be 1.865 Å and 1.757 Å for the Fe<sup>III</sup> and Fe<sup>IV</sup> site, respectively. This clearly reveals a strong valence localisation enforced due to strong structural distortions around the Fe<sup>IV</sup>=O unit. The terminal Fe-O(2)H(O1) distance is found to be 1.828 Å (1.641 Å) (see Fig. 1a). Our computed data are in agreement with earlier theoretical results and experiments.<sup>46,67,73</sup>

The Wiberg bond index<sup>142</sup> computed for Fe<sup>III</sup>- $\mu$ O and Fe<sup>IV</sup>- $\mu$ O is 0.62 and 0.80, respectively, revealing a single bond character between Fe and  $\mu$ O centres. The Wiberg bond index for the terminal Fe<sup>III</sup>-O(2) and Fe<sup>IV</sup>-O(1) is estimated to be 0.62 and 1.30, revealing single and double bond characters for Fe<sup>III</sup> and Fe<sup>IV</sup> centres, respectively. Natural bond orbital (NBO) analysis (see also Fig. S5 in the ESI†) reveals that the ionicity of the Fe<sup>IV</sup>- $\mu$ O bond is smaller compared to the Fe<sup>III</sup>- $\mu$ O bond. The spin natural orbitals (SNOs) with atomic spin density values estimated for  $^2\mathbf{1}_{\text{hs-hs}}$  (see Fig. S6 in the ESI†) reveal four  $\beta$ -spin (five  $\alpha$ -spin) electrons for the Fe<sup>IV</sup> (Fe<sup>III</sup>) centre. The high-spin Fe<sup>IV</sup> centre undergoes pseudo-Jahn-Teller distortion (axial compression) possessing a longer Fe-N(L) distance and shorter



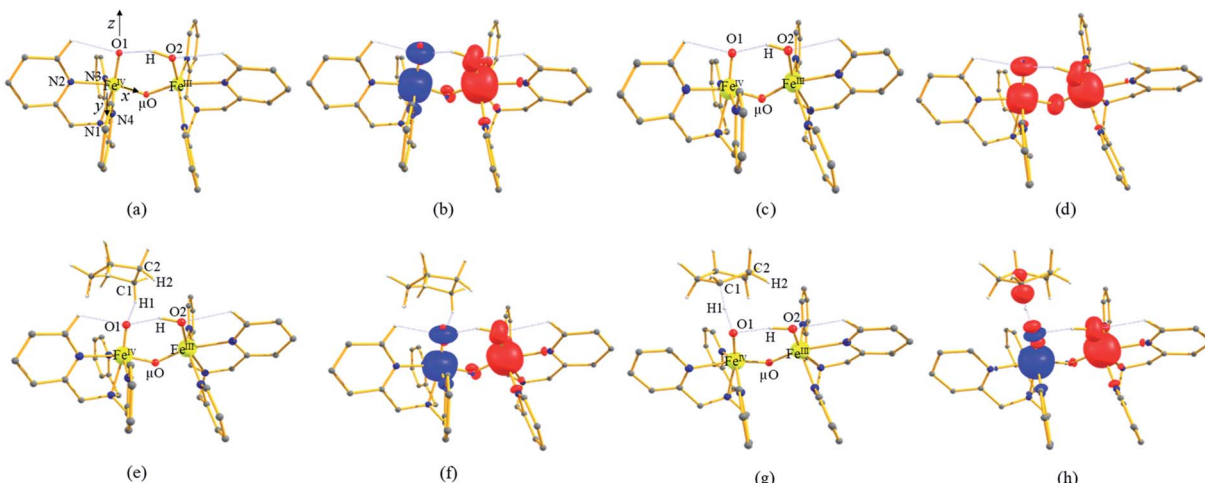


Fig. 1 (a and b) The optimized structure of  $^{21}_{\text{hs-hs}}$  and its corresponding spin density plot, (c and d) optimized structure of  $^{10}_{\text{hs-hs}}$  and its corresponding spin density plot, (e and f) optimized structure of  $^{2}\text{RC}_{\text{hs-hs}}$  and its corresponding spin density plot and (g and h) optimized structure of  $^{2}\text{TS}_{\text{Hhs-hs}}$  and its corresponding spin density plot. Some important structural parameters computed for the spin states and spin density values are given below for species **1**, RC and I-TS<sub>H</sub>. For spin state  $^{21}_{\text{hs-hs}}$ , Fe<sup>IV</sup>–O1 = 1.641, Fe<sup>III</sup>–O2 = 1.828, Fe<sup>IV</sup>–μO = 1.757, Fe<sup>III</sup>–μO1 = 1.865, O2–H = 0.984, and O1–H = 1.856 and spin density Fe<sup>IV</sup> = –3.04, Fe<sup>III</sup> = 3.99, O1 = –0.48, O2 = 0.38, and μO = 0.05. For spin state  $^{10}_{\text{hs-hs}}$ , Fe<sup>IV</sup>–O1 = 1.642, Fe<sup>III</sup>–O2 = 1.834, Fe<sup>IV</sup>–μO = 1.778, Fe<sup>III</sup>–μO1 = 1.901, O2–H = 0.981, and O1–H = 1.901 and spin density Fe<sup>IV</sup> = 3.04, Fe<sup>III</sup> = 4.04, O1 = 0.56, and O2 = 0.39, μO = 0.42. For spin state  $^{2}\text{RC}_{\text{hs-hs}}$ , Fe<sup>IV</sup>–O1 = 1.639, Fe<sup>III</sup>–O2 = 1.825, Fe<sup>IV</sup>–μO = 1.757, Fe<sup>III</sup>–μO1 = 1.866, O1–H1 = 2.575, H1–C1 = 1.097,  $\angle$ Fe<sup>IV</sup>–O1–H1 = 112°, and  $\angle$ O1–H1–C1 = 120° and spin density Fe<sup>IV</sup> = –3.04, Fe<sup>III</sup> = 3.99, O1 = –0.48, O2 = 0.38, μO = 0.05, and C1 = 0.00. For spin state I– $^{2}\text{TS}_{\text{Hhs-hs}}$ , Fe<sup>IV</sup>–O1 = 1.752, Fe<sup>III</sup>–O2 = 1.835, Fe<sup>IV</sup>–μO = 1.805, Fe<sup>III</sup>–μO1 = 1.826, O1–H1 = 1.303, H1–C1 = 1.230,  $\angle$ Fe<sup>IV</sup>–O1–H1 = 157°, and  $\angle$ O1–H1–C1 = 170° and spin density Fe<sup>IV</sup> = –3.87, Fe<sup>III</sup> = 3.97, O1 = 0.02, O2 = 0.38, μO = 0.00, and C1 = 0.39. All bond lengths are given in Å and angles are given in °. All hydrogen atoms (except O2–H, C1–H1, and C2–H2) are omitted for clarity.

Fe<sup>IV</sup>–O(1) distance (see Table S4a in the ESI<sup>†</sup>). These distortions in the coordination environment of Fe<sup>IV</sup> lead to a pure valence localisation picture, as stated earlier,<sup>8</sup> and is supported by the computed spin density plots (see Fig. 1b). The bridging μO atom has net positive spin density reflecting stronger delocalisation of spins from the dominant  $\alpha$  carrier Fe<sup>III</sup> while the terminal hydroxo/oxo (0.38/–0.48) group is found to have strong delocalisation of spins from the metal centre<sup>143</sup> (see Table S5a in the ESI<sup>†</sup>). Of particular relevance is the spin density of the terminal oxygen connected to the Fe<sup>IV</sup> unit, where significant negative spin density is detected, revealing an oxyl radical character that is responsible for the high reactivity of such species earlier.<sup>67,72,144</sup>

The second most important state is  $^{10}_{\text{hs-hs}}$  that lies very close to the ground state and corresponds to a ferromagnetic coupling between high-spin Fe<sup>III</sup> and Fe<sup>IV</sup> centres. Here the geometry is very similar to  $^{21}_{\text{hs-hs}}$ , with a notable difference being slightly longer Fe<sup>IV</sup>–O(1) distances (1.642 Å) (see Fig. 1c and Table S4a in the ESI<sup>†</sup>). Computed spin density values for the first excited spin state ( $^{10}_{\text{hs-hs}}$ ) with respect to  $^{21}_{\text{hs-hs}}$  on the Fe<sup>IV</sup> and Fe<sup>III</sup> were found to be 3.04 and 4.04, respectively (see Fig. 1d) also suggesting a valence localisation of the spins. The magnetic coupling of the complex **1** for a high spin ( $S = 2$  and  $S = 5/2$ ) is computed using the ground state structure employing the standard protocol,<sup>145</sup> and this gives a  $J$  value of  $-137.3 \text{ cm}^{-1}$ , and this matches well with the experimental estimate of  $-90 \pm 20 \text{ cm}^{-1}$  reported using EPR studies<sup>73</sup> offering confidence in the estimated structures and properties. Here, we have computed the overlap integral between two SOMOs of the Fe centres<sup>108</sup> and

a significant overlap is noted between the SOMOs of  $d_{yz}$  and  $d_{xz}$  orbitals of Fe<sup>III</sup> and Fe<sup>IV</sup> centres, respectively, and this strong overlap is found to be responsible for the strong antiferromagnetic coupling observed (see Tables S6 and S7 in the ESI<sup>†</sup>). In the subsequent section, the reactivity of species **1** is discussed towards cyclopentane as a substrate for the hydroxylation and desaturation reaction. We discuss first the 1<sup>st</sup> hydrogen abstraction from cyclopentane as a substrate and later expand the mechanism to hydroxylation *vs.* desaturation pathways as discussed earlier.

### First hydrogen atom abstraction

Based on reported experimental evidence on **1** and related studies, we have adapted various mechanistic pathways for the hydroxylation and dehydrogenation reaction,<sup>120,146,147</sup> as shown in Scheme 2. The first hydrogen atom abstraction can be due to (i) the terminal Fe<sup>IV</sup>–O(1) centre (pathway I) (ii) or by the μ-oxo bridge that lies between the Fe<sup>IV</sup> and Fe<sup>III</sup> centres (pathway II) (iii) or by the terminal Fe<sup>III</sup>–O(2)H species (pathway III). The individual pathways assumed are further diverged into either hydroxylation that can happen *via* rebound or second hydrogen atom abstraction leading to desaturation. In pathway I, the first hydrogen atom abstraction from cyclopentane *via* the transition state (I-TS<sub>H</sub>) leads to the formation of the radical intermediate (**I-Int**).

This radical intermediate can either undergo the –OH rebound step *via* **Ia-TS<sub>reb</sub>** and yield the hydroxylated product (**Ia-P<sub>reb</sub>**; pathway Ia) or undergo second hydrogen abstraction *via* **Ib-TS<sub>2H</sub>** leading to cyclopentene (**Ib-P<sub>2H</sub>**; pathway Ib). Additionally,

the second hydrogen atom could also be abstracted by the  $\mu$ -oxo bridge present at the **I-Int** *via* **Ic-TS<sub>2H</sub>** (pathway Ic), leading to desaturation. In pathway II, the hydrogen abstraction by the  $\mu$ -oxo bridge led to **II-Int**, and this in the subsequent step undergoes  $-\mu\text{OH}$  rebound hydroxylation leading to the hydroxylated product. In pathway III, the first hydrogen atom abstraction leads to **III-Int**, which subsequently undergoes second hydrogen atom abstraction (*via* **III-TS<sub>2H</sub>**) by the terminal  $\text{Fe}^{\text{IV}}=\text{O}(1)$  leading to the desaturated product.

The computed potential energy surface (PES) for the oxidation of cyclopentane is shown in Fig. 2 (pathway I). In the first step, a weak reactant complex formation is assumed with the substrate, and the  $\text{O}\cdots\text{H}$  interaction between  $\text{O}(1)$  and a hydrogen atom of the substrate. We have computed nine possible spin states with  ${}^2\text{RC}_{\text{hs-hs}}$  as the ground state, with the  ${}^{10}\text{RC}_{\text{hs-hs}}$ ,  ${}^8\text{RC}_{\text{hs-is}}$ ,  ${}^4\text{RC}_{\text{hs-is}}$ ,  ${}^6\text{RC}_{\text{is-is}}$ ,  ${}^2\text{RC}_{\text{is-is}}$ ,  ${}^4\text{RC}_{\text{ls-is}}$ ,  ${}^2\text{RC}_{\text{ls-is}}$ , and  ${}^2\text{RC}_{\text{ls-ls}}$  states lying at 0.9, 23.2, 18.9, 60.2, 58.7, 85.1, 85.3 and 164.6  $\text{kJ mol}^{-1}$ , respectively. Formation of species **RC** from the reactant is found to be slightly exothermic by  $-18.1 \text{ kJ mol}^{-1}$  justifying the need to invoke such complex formation. The optimised structures are similar to the ground state structure estimated with some minor alterations (see Fig. 1e and f and Table S4a<sup>†</sup> for structural parameters, and spin density Table S5a in the ESI<sup>†</sup>). The  $\text{O}(1)\text{-H}(1)$  and  $\text{C}(1)\text{-H}(1)$  bond distances of the  ${}^2\text{RC}_{\text{hs-hs}}$  state are computed to be 2.575  $\text{\AA}$  and 1.097  $\text{\AA}$ , respectively.

In pathway I, our computed results show that the **I-<sup>2</sup>TS<sub>Hhs-hs</sub>** is the lowest-lying with an extremely small barrier height of 38.3  $\text{kJ mol}^{-1}$  while the **I-<sup>10</sup>TS<sub>Hhs-hs</sub>**, **I-<sup>8</sup>TS<sub>Hhs-is</sub>**, **I-<sup>4</sup>TS<sub>Hhs-is</sub>**, **I-<sup>6</sup>TS<sub>His-is</sub>**, **I-<sup>2</sup>TS<sub>His-is</sub>**, **I-<sup>4</sup>TS<sub>His-is</sub>**, **I-<sup>2</sup>TS<sub>His-ls</sub>** and **I-<sup>2</sup>TS<sub>His-ls</sub>** transition states lie higher at 62.2, 125.6, 124.0, 141.0, 148.0, 188.9, 193.8, and 205.5  $\text{kJ mol}^{-1}$  respectively with respect to **RC**.

Clearly, all the spin states are higher in energy and the reactivity at this step is dictated by the antiferromagnetically coupled states of high-spin  $\text{Fe}^{\text{III}}$  and  $\text{Fe}^{\text{IV}}$  centres with a small but a finite possibility of the ferromagnetically coupled state also participating in the mechanism. From the reactant, the barrier is merely 20.2  $\text{kJ mol}^{-1}$ , revealing an extremely low barrier height to activate relatively inert substrates such as cyclopentane, and this is consistent with the million-fold reactivity order observed in the experiments. The lower barrier height observed for the **I-<sup>2</sup>TS<sub>Hhs-hs</sub>** species suggests a possible two-state reactivity scenario as noted for mononuclear  $\text{Fe}^{\text{IV}}=\text{O}$  complexes.<sup>52,53</sup> However, the stark difference here is that these states arise due to the difference in exchange coupling and therefore are expected to be very close-lying in energy. The optimised structure of the **I-<sup>2</sup>TS<sub>Hhs-hs</sub>** for the C-H bond activation is shown in Fig. 1g. For the **I-<sup>2</sup>TS<sub>Hhs-hs</sub>** species, the  $\text{Fe}^{\text{IV}}\text{-O}(1)$  bond length is found to be elongated to 1.752  $\text{\AA}$  from 1.639  $\text{\AA}$  and the  $\text{C}(1)\text{-H}(1)$  bond to 1.230  $\text{\AA}$  from 1.097  $\text{\AA}$  (see Fig. 1e and g and S9<sup>†</sup>). The  $\text{O}(1)\text{-H}(1)\text{-C}(1)$  (cyclopentane) bond angle is determined to be  $170^\circ$  while the  $\text{Fe}^{\text{IV}}\text{-O}(1)\text{-H}(1)$  angle is found to be  $157^\circ$ . The lengthening of the bond in the  $\text{C-H}\cdots\text{O}1$  interaction (2.425  $\text{\AA}$  from 2.312  $\text{\AA}$ ) in **I-TS<sub>H</sub>** reflects the fact that the oxyl group has lower electron-donating capability relative to the more negatively charged oxo ligand. This step is found to be the rate-determining step for both alkene and hydroxylation reactions (see below). As expected for the  $\text{Fe}^{\text{IV}}=\text{O}(1)$  group, the reaction takes place at the  $\text{Fe}^{\text{IV}}=\text{O}(1)$  unit and proceeds *via* the  $\sigma$  channel, and this mechanism has been well-established for mononuclear  $\text{Fe}^{\text{IV}}=\text{O}$  complexes.<sup>148-150</sup> In the  $\sigma$  channel, one electron from the substrate that has the same spin as the remaining electrons in the  $\text{Fe}^{\text{IV}}$  centre is transferred into the  $\sigma^*(\text{Fe}=\text{O})$  antibonding orbital during C-H bond activation by

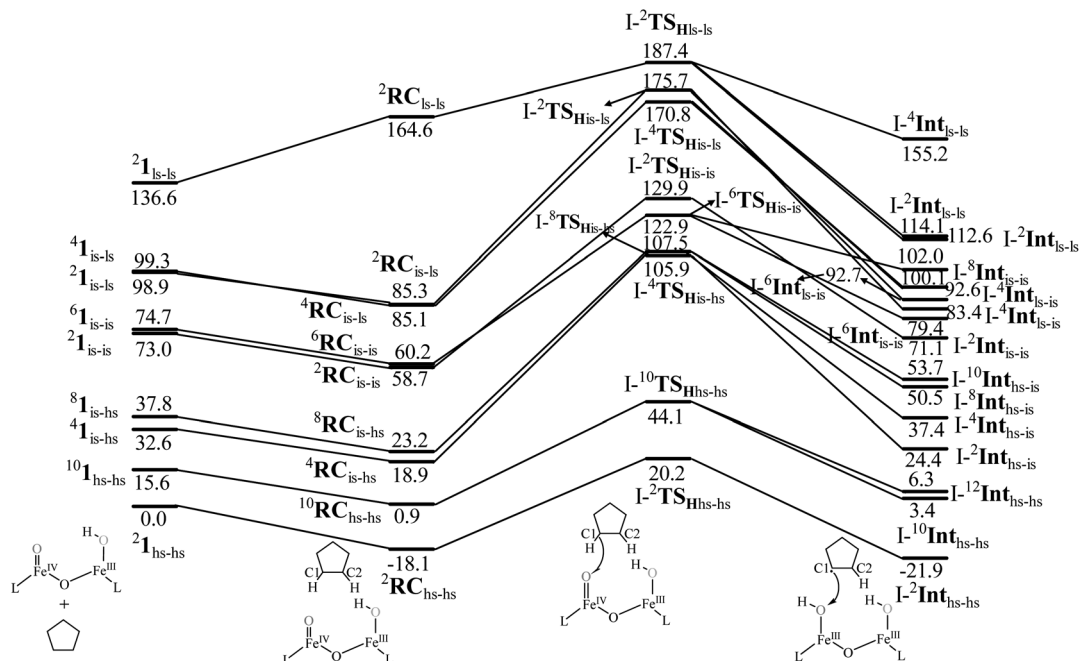


Fig. 2 B3LYP-D3 computed energy for the C-H bond hydroxylation of cyclopentane (CP) by species **1** (energies are in  $\text{kJ mol}^{-1}$ ).



a high-spin  $\text{Fe}^{\text{IV}}=\text{O}(1)$  centre. One of the most important characteristic features that occur upon approaching the transition state is the  $\text{Fe}^{\text{IV}}-\text{O}(1)-\text{H}(1)$  angle in  $\mathbf{I}\text{-TS}_{\text{H}}$ , and these angles for the  $\sigma$ -pathway are close to  $180^\circ$ .<sup>151-153</sup> An analysis of the group spin densities and charges (based on Mulliken analysis) indicates that cyclopentane at  $\mathbf{I}\text{-}^2\text{TS}_{\text{Hhs-hs}}$  has a radical character with the group spin density estimated to be  $\rho_{\text{C}(1)} = 0.39$  (where  $\rho$  = spin density) with small overall charge (group charge  $Q_{\text{C}(1)} = -0.12$ ). The spin values on the  $\text{H}(1)$  (transferred hydrogen) increase from 0.00 to 0.02 at the transition state but at the same time, the electron shifts to the  $\text{Fe}-\sigma_{z^2}^*$  orbital of  $\text{Fe}^{\text{IV}}=\text{O}(1)$  leading to attenuation of spin density from  $-0.48$  to  $0.02$  in  $\mathbf{I}\text{-}^2\text{TS}_{\text{Hhs-hs}}$  at the oxo centre. The spin density on the iron ion in  $\mathbf{I}\text{-}^2\text{TS}_{\text{Hhs-hs}}$  increases from  $-3.03$  to  $-3.78$ . The change in the spin density value suggests a  $\beta$ -electron transfer from the substrate to the  $\text{Fe}^{\text{IV}}-\sigma_{z^2}^*$  orbital of the  $\text{Fe}^{\text{IV}}$  centre accompanied by  $\text{Fe}^{\text{IV}}$  attaining the +3 oxidation state (see Fig. 3).<sup>153,154</sup> Thus, the proposed mechanism consists of a Proton-Coupled Electron Transfer (PCET) process from the substrate<sup>115,155</sup> to the  $\text{Fe}^{\text{IV}}$  centre. Fig. 3 shows the electron-shift diagram for the PCET step for both doublet and decet spin states with interacting orbitals and SNOs occupation. In the RC, the  $\text{Fe}^{\text{III}}$  iron centres of the doublet and decet have five unpaired  $\alpha$  electrons in the d-orbital.

The  $\text{Fe}^{\text{IV}}=\text{O}(1)$  ( $S_b$ ) centre has four unpaired electrons which have spin-up  $\alpha$  orientation in  ${}^2\text{RC}_{\text{hs-hs}}$  and  $\beta$  orientation in the  ${}^2\text{RC}_{\text{hs-hs}}$ . At the  $\mathbf{I}\text{-}^2\text{TS}_{\text{Hhs-hs}}$  and  $\mathbf{I}\text{-}^2\text{TS}_{\text{Hhs-hs}}$  transition states,

one electron is transferred to the  $\text{Fe}^{\text{IV}} \sigma^*(\text{d}_z^2)$  orbital and the spin orientation of the transferred electron is  $\beta$  and  $\alpha$ , respectively for the  $\mathbf{I}\text{-}^2\text{TS}_{\text{Hhs-hs}}$  and  $\mathbf{I}\text{-}^2\text{TS}_{\text{Hhs-hs}}$  transition states. Even though the PCET step of both the spin-states offers exchange-enhanced reactivity (EER) stabilisation,<sup>137,152,156,157</sup> this is likely to be larger for the doublet state than for the decet state. Also, at the transition state, the  $\phi_{\text{C}}$  and  $\text{d}_{x^2-y^2}$  orbitals are found to have significant overlap revealing retention of the estimated antiferromagnetic coupling at the reactant level (see Tables S8 and S9 in the ESI†).

To further understand the nature of the hydrogen transfer mechanism, we have constructed a thermodynamic cycle considering PCET (proton-coupled electron transfer), PT-ET (proton transfer followed by electron transfer), and ET-PT (electron transfer followed by proton transfer) pathways (see Fig. 4).<sup>93,95,97,98</sup> Our calculations reveal a significant energy penalty for the PT-ET and ET-PT steps. Further spin density values (see Fig. 1h and 5) indicate that the transition state resembles  $\text{Fe}^{\text{III}}-\text{OH}$  species suggesting the PCET type mechanism as revealed by the computed energetics. Additionally, the mechanism can also be differentiated by computing deformation energies ( $\Delta E_{\text{def}}$ ) at the transition state and comparing it against the gas-phase barrier ( $\Delta E^\ddagger$ ) and interaction energies ( $\Delta E_{\text{int}}$ ) as stated earlier by Shaik and co-workers.<sup>115</sup> Our calculated  $\Delta E^\ddagger$ ,  $\Delta E_{\text{def}}$ , and  $\Delta E_{\text{int}}$  values are  $59.9$ ,  $22.7$ , and  $36.0$   $\text{kJ mol}^{-1}$ , respectively revealing  $\Delta E_{\text{def}} < \Delta E^\ddagger$  and  $\Delta E_{\text{int}} > 0$  scenarios and thus strongly favouring PCET processes of the C-H bond of cyclopentane and not HAT (also see ESI† for additional text on PCET vs. HAT).<sup>115</sup>

To further understand the electronic co-operation between the two metal centres, we have replaced the neighbouring  $\text{Fe}^{\text{III}}$  ion by  $\text{Co}^{\text{III}}$  and  $\text{Ga}^{\text{III}}$  ions and computed the corresponding transition state at the  $S = 2$  surface. The barrier height estimated for this fictitious model is found to be  $44.4$  and  $31.3$   $\text{kJ mol}^{-1}$  with respect to the reactant (see Fig. S10 and S11 in the ESI†) for  $\text{Co}^{\text{III}}$  and  $\text{Ga}^{\text{III}}$  substitutions, respectively. This barrier height computed is higher compared to the  $\text{Fe}^{\text{III}}$  centre revealing the importance of spin-cooperation in dictating the reactivity of species **1**. This barrier height computed for the fictitious  $[\text{HO}(\text{L})\text{Co}^{\text{III}}-\text{O}-\text{Fe}^{\text{IV}}(\text{O})(\text{L})]^{2+}$  models is similar to the estimate found for mononuclear enzyme TauD as well as the model catalysts  $[\text{TpOBzFe}^{\text{IV}}=\text{O}]$ , for the first hydrogen atom abstraction from cyclopentane where spin-cooperation is absent.<sup>66</sup>

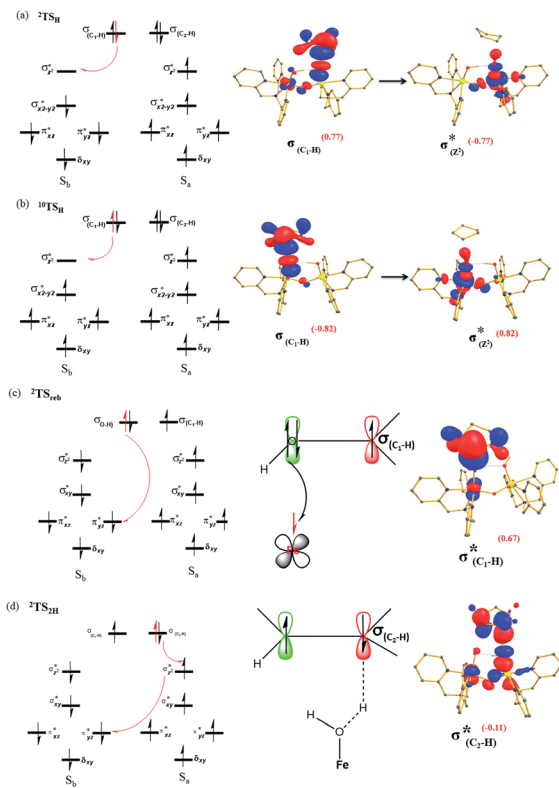


Fig. 3 Electron shift diagrams of  $\mathbf{I}\text{-TS}_{\text{H}}$  for both (a)  $\mathbf{I}\text{-}^2\text{TS}_{\text{Hhs-hs}}$ , (b)  $\mathbf{I}\text{-}^2\text{TS}_{\text{Hhs-hs}}$ , (c)  $\mathbf{I}\text{-}^2\text{TS}_{\text{rebhs-hs}}$  and (d)  $\mathbf{I}\text{-}^2\text{TS}_{\text{2Hhs-hs}}$  with SNOs and their occupation (noted in parentheses).

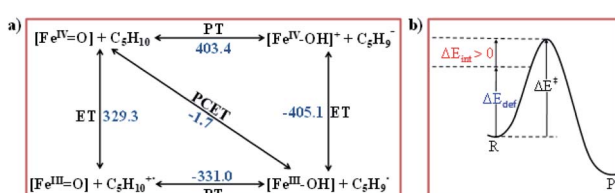


Fig. 4 (a) Relative thermodynamic free energies between the  $\text{Fe}^{\text{IV}}=\text{O}$  unit and its hydroxo complexes (all energies are in  $\text{kJ mol}^{-1}$ ) and (b) the relationship between the barrier ( $\Delta E^\ddagger$ ), the deformation energy of reactant ( $\Delta E_{\text{def}}$ ) and the interaction energy  $\Delta E_{\text{int}}$  at the transition state:  $\Delta E_{\text{int}} > 0$ .



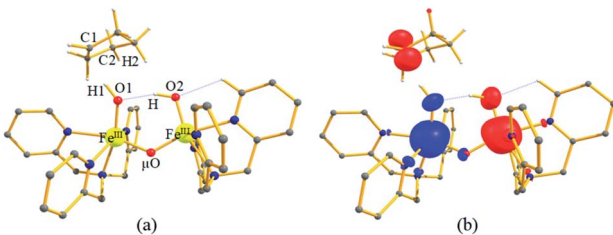


Fig. 5 (a and b) The optimised structure of  $\text{I-}^2\text{Int}_{\text{hs-hs}}$  and its corresponding spin density plot. Some important structural parameters computed for the spin states and spin density values are given below for species **I-Int**. For spin state  $\text{I-}^2\text{Int}_{\text{hs-hs}}$ ,  $\text{Fe}^{\text{III}}-\text{O}1 = 1.854$ ,  $\text{Fe}^{\text{III}}-\text{O}2 = 1.835$ ,  $\text{Fe}^{\text{III}}-\mu\text{O} = 1.806$ ,  $\text{Fe}^{\text{III}}-\mu\text{O}1 = 1.825$ ,  $\text{O}1-\text{H}1 = 0.981$ ,  $\text{H}1-\text{C}1 = 2.012$ ,  $\angle \text{Fe}^{\text{III}}-\text{O}1-\text{H}1 = 129^\circ$ , and  $\angle \text{O}1-\text{H}1-\text{C}1 = 167^\circ$  and spin density  $\text{Fe}^{\text{III}} = -3.97$ ,  $\text{Fe}^{\text{III}} = 3.96$ ,  $\text{O}1 = -0.25$ ,  $\text{O}2 = 0.38$ ,  $\mu\text{O} = -0.07$ , and  $\text{C}1 = 0.93$ . All the distances are given in Å and angles in  $^\circ$ . All hydrogen atoms (except  $\text{O}2-\text{H}$ ,  $\text{C}1-\text{H}1$ , and  $\text{C}2-\text{H}2$ ) are omitted for clarity.

A hydrogen atom abstraction leads to an intermediate  $\{(\text{OH})\text{Fe}^{\text{III}}-\mu(\text{O})-\text{Fe}^{\text{III}}(\text{OH})\}$  (**I-Int**). Considering the exchange interaction between  $S_a$  and  $S_b$  iron centres and spin on the cyclopentyl radical coupled to the unpaired electrons on both iron centres, there are seventeen possible spin states, and we have computed all spin states for this species. Compared to the reactant energies, the  $\text{I-}^2\text{Int}_{\text{hs-hs}}$  state is found to be the lowest-lying at  $-21.9 \text{ kJ mol}^{-1}$  (see Fig. 5a and b) followed by  $\text{I-}^{12}\text{Int}_{\text{hs-hs}}$ ,  $\text{I-}^{10}\text{Int}_{\text{hs-hs}}$ ,  $\text{I-}^{10}\text{Int}_{\text{hs-is}}$ ,  $\text{I-}^8\text{Int}_{\text{hs-is}}$ ,  $\text{I-}^4\text{Int}_{\text{hs-is}}$ ,  $\text{I-}^2\text{Int}_{\text{hs-is}}$ ,  $\text{I-}^8\text{Int}_{\text{is-is}}$ ,  $\text{I-}^6\text{Int}_{\text{is-is}}$ ,  $\text{I-}^2\text{Int}_{\text{is-is}}$ ,  $\text{I-}^2\text{Int}_{\text{is-is}}$ ,  $\text{I-}^6\text{Int}_{\text{is-is}}$ ,  $\text{I-}^4\text{Int}_{\text{is-is}}$ ,  $\text{I-}^4\text{Int}_{\text{is-is}}$  and  $\text{I-}^2\text{Int}_{\text{is-is}}$  states at  $6.3$ ,  $3.4$ ,  $53.7$ ,  $50.5$ ,  $37.4$ ,  $24.4$ ,  $100.0$ ,  $79.4$ ,  $71.1$ ,  $155.2$ ,  $114.0$ ,  $112.6$ ,  $92.7$ ,  $92.6$ ,  $83.4$  and  $87.3 \text{ kJ mol}^{-1}$  energies, respectively. As spin-down electron shifts from  $\sigma(\text{C}(1)-\text{H}(1))$  to the metal centre, a spin-up radical character develops at the surface as revealed by significant spin density at the carbon centre in all the intermediates computed ( $\rho_{\text{C}(1)} = 0.93$  for  $\text{I-}^2\text{Int}_{\text{hs-hs}}$  with  $Q_{\text{C}(1)} = 0.04$  and see Fig. S12 in the ESI† for the orbital interaction diagram). The calculated energies reveal that  $\text{I-}^2\text{Int}_{\text{hs-hs}}$  is thermodynamically stable ( $28.2 \text{ kJ mol}^{-1}$ ) relative to  $\text{I-}^{12}\text{Int}_{\text{hs-hs}}$ , and this is the manifestation of antiferromagnetic interaction between the metal centres. As we move from left to right in Fig. 2, the strength of antiferromagnetic coupling is enhanced and this is due to the addition of a  $\beta$  electron to the  $\sigma^*(\text{d}_z^2)$  at the  $S_b$  iron centre in the doublet state which maximises the d- orbital overlap between the two Fe centres (see Fig. S13 in the ESI†).

In pathway II, the barrier for the first hydrogen atom abstraction by the  $\mu$ -oxo bridge is found to be  $160.1 \text{ kJ mol}^{-1}$  with respect to the **RC**, and this is nearly eight times larger than the transition state computed using pathway I at the doublet surface (see Fig. 8). The optimised structure and spin density plot of the  $\text{II-}^2\text{RC}_{\text{hs-hs}}$ ,  $\text{II-}^2\text{TS}_{\text{Hhs-hs}}$ , and  $\text{II-}^2\text{Int}_{\text{hs-hs}}$  are shown in Fig. S14a-f in the ESI†. Here at the  $\text{II-}^2\text{TS}_{\text{H}}$ , the  $\text{Fe}^{\text{IV}}-\text{O}(1)-\text{H}(1)$  angle is found to be  $106^\circ$  revealing  $\pi$  type reactivity as the substrate is hindered and cannot approach in a linear fashion as required for a lower barrier  $\sigma$  channel observed in pathway I (see Fig. S15a in the ESI†). The first hydrogen atom abstraction leads to the formation of the **II-Int**  $[\text{HO}(\text{L})\text{Fe}^{\text{III}}-\text{O}-\text{Fe}^{\text{III}}(\text{O})(\text{L})]^{2+}$

intermediate. The formation of this species is found to be endothermic by  $60.1 \text{ kJ mol}^{-1}$ . As the two Fe centres are anti-ferromagnetically coupled, the spin density at the  $\mu$ -oxo bridge is found to be only  $0.05$ , suggesting a significantly reduced radical character (compared to ferryl-oxygen in the  $\text{Fe}^{\text{IV}}=\text{O}(1)$  unit) and hence a larger barrier height. This suggests that when both terminal and bridge  $\mu$ -oxo are present in the complex, the reactivity is expected to occur *via* the terminal  $\text{Fe}^{\text{IV}}=\text{O}$  unit. Also, in enzymes such as sMMO where bis  $\mu$ -oxo bridged dimers are proposed, the reactivity may be triggered by the open-ended structure where the  $\mu$ -oxo bridge first undergoes cleavage to generate a terminal  $\text{Fe}^{\text{IV}}=\text{O}(1)$  unit followed by hydrogen atom abstraction as has been suggested very recently.<sup>13</sup>

In pathway III, the first hydrogen abstraction by the terminal  $\text{Fe}^{\text{III}}-\text{O}(2)\text{H}$  is estimated to have a barrier of  $126.2 \text{ kJ mol}^{-1}$ , which is nearly six times larger compared to the terminal  $\text{Fe}^{\text{IV}}=\text{O}(1)$  group considered in pathway I at the doublet surface (see Fig. 6). The optimised structure and spin density plot of the  $\text{III-}^2\text{TS}_{\text{Hhs-hs}}$  and  $\text{III-}^2\text{Int}_{\text{hs-hs}}$  are shown in Fig. S16a-d in the ESI†. The  $\text{Fe}^{\text{III}}-\text{O}(2)-\text{H}(1)$  angle here is found to be  $130^\circ$  revealing a  $\pi$ -type pathway as the linear approach is restricted by the additional hydrogen atom present (see Fig. S15b†). Besides as  $\text{Fe}^{\text{III}}$  is an exchange saturated state and poorer electrophile compared to  $\text{Fe}^{\text{IV}}=\text{O}$  species as revealed by a significantly less radical character (spin density of  $0.38$  at the oxygen atom of the -OH group) the barrier height estimated is in line with the expectation. The abstraction of the hydrogen atom leads to the formation of **III-Int**, which in the subsequent step is expected to undergo second hydrogen atom abstraction by the terminal  $\text{Fe}^{\text{IV}}=\text{O}(1)$  unit leading to the desaturated product. The formation of **III-Int** is endothermic by  $78.6 \text{ kJ mol}^{-1}$ .

It is important to note here that the substitution of the -OH group by -F in the  $\text{Fe}^{\text{III}}$  centre was found to enhance the reactivity significantly.<sup>67,158</sup> We also performed additional calculations on the  $[\text{F}(\text{L})\text{Fe}^{\text{III}}-\text{O}-\text{Fe}^{\text{IV}}(\text{O})(\text{L})]^{2+}$  species to see if the spin-cooperation discussed is visible upon substitution by -F

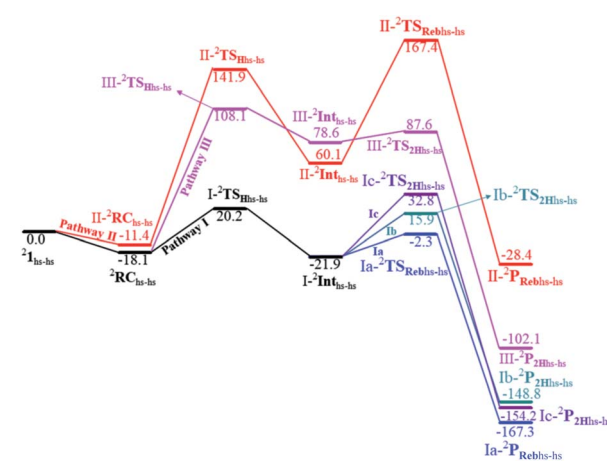


Fig. 6 Potential energy surface computed (energies are in  $\text{kJ mol}^{-1}$ ) for C–H activation of cyclopentane by species  $^2\text{1}_{\text{hs-hs}}$  comparing the lowest estimate of barrier heights obtained from various pathways computed in Scheme 2.



and our orbital analysis reveals that there is significant overlap between the d-orbitals of the two Fe centres suggesting strong spin-cooperation (see Fig. S17a–c in the ESI†). Due to strong hydrogen bonding interactions, compound **1** was found to have a *syn* conformation as its ground state, while the  $[\text{F}(\text{L})\text{Fe}^{\text{III}}-\text{O}-\text{Fe}^{\text{IV}}(\text{O})(\text{L})]^{2+}$  complex was found to have an *anti* conformation as its ground state. This significantly reduces the steric strain of the substrate approaching the complex, lowering the barrier height. This has been explored thoroughly earlier by Neese *et al.*<sup>67</sup>

### Hydroxylation vs. desaturation

In the next step of pathway I, there are three possible pathways (i) rebound of the O–H group to the cyclopentyl radical (pathway Ia) or (ii) second hydrogen abstraction from the cyclopentyl radical (pathway Ib) by the terminal  $\text{Fe}^{\text{III}}-\text{O}(1)\text{H}(1)$  group (see Scheme 2) or (iii) second hydrogen abstraction by the  $\mu$ -oxo bridge from the cyclopentyl radical (pathway Ic).<sup>66,159</sup> Here, all three steps have a common intermediate species, which is generated by the hydrogen abstraction from the C(1)–H(1) bond of cyclopentane. The  $\text{Fe}^{\text{III}}-\text{OH}$  intermediate species has the capability to perform –OH rebound to yield hydroxylation or can abstract the second hydrogen atom leading to the desaturation product. Various factors dictate how the reaction diverges from the intermediate. Here in this example studied, it is capable of performing both the reactions suggesting that the barrier height for –OH rebound and desaturation are likely to be affordable unlike in other dinuclear Fe(*v*)-oxo dimers where –OH rebound has not been witnessed.<sup>13</sup> The divergence is

dictated by many factors such as the nature of the  $\text{Fe}=\text{O}$  bond, the organic substrate, the steric hindrance, the coordinated ligands, the spin state during the reaction pathways, and the nature of magnetic coupling that exists between the two metal centres. The conversion of the cyclopentyl radical to the corresponding cyclopentanol through the rebound pathway (pathway Ia) is shown in Scheme 2. We have calculated  $\text{Ia}^{-12}\text{TS}_{\text{rebhs-hs}}$ ,  $\text{Ia}^{-10}\text{TS}_{\text{rebhs-hs}}$ ,  $\text{Ia}^{-2}\text{TS}_{\text{rebhs-hs}}$ ,  $\text{Ia}^{-10}\text{TS}_{\text{rebhs-is}}$ ,  $\text{Ia}^{-8}\text{TS}_{\text{rebhs-is}}$ ,  $\text{Ia}^{-4}\text{TS}_{\text{rebhs-is}}$ ,  $\text{Ia}^{-2}\text{TS}_{\text{rebhs-is}}$ ,  $\text{Ia}^{-8}\text{TS}_{\text{rebis-is}}$ ,  $\text{Ia}^{-6}\text{TS}_{\text{rebis-is}}$ ,  $\text{Ia}^{-2}\text{TS}_{\text{rebis-is}}$ ,  $\text{Ia}^{-4}\text{TS}_{\text{rebis-is}}$ ,  $\text{Ia}^{-2}\text{TS}_{\text{rebis-is}}$ ,  $\text{Ia}^{-2}\text{TS}_{\text{rebis-is}}$ ,  $\text{Ia}^{-4}\text{TS}_{\text{rebis-is}}$ ,  $\text{Ia}^{-2}\text{TS}_{\text{rebis-is}}$  and  $\text{Ia}^{-2}\text{TS}_{\text{rebis-is}}$  transitions states and  $\text{Ia}^{-2}\text{TS}_{\text{rebhs-hs}}$  is found to be the lowest in energy which is found to be  $19.6 \text{ kJ mol}^{-1}$  followed by  $146.1, 49.1, 78.3, 98.7, 79.8, 74.4, 142.7, 143.8, 140.5, 187.5, 198.4, 206.2, 177.5, 157.1, 152.1$ , and  $180.7 \text{ kJ mol}^{-1}$  respectively with respect to the **I-Int** (see Fig. 7).

In  $\text{Ia}^{-2}\text{TS}_{\text{rebhs-hs}}$ , the  $\alpha$  electron of  $\phi(\text{C}1)$  has to transfer to the  $\pi_{xy/yz}^*$  of the  $\text{Fe}^{\text{III}}(\text{S}_b)$  iron centre to form coordinated cyclopentanol with the  $\text{Fe}^{\text{II}}(\text{S}_b)$  iron centre (see Fig. 8a and b, 3c and S18 in the ESI†). As the  $\text{Ia}^{-10}\text{TS}_{\text{rebhs-hs}}$  state already has all the  $\alpha$  d-orbitals occupied, it can only accept a  $\beta$  electron from the  $\phi(\text{C}1)$  to the  $\pi_{xy/yz}^*$  of the  $\text{Fe}^{\text{III}}(\text{S}_b)$  centre. This leads to a reduction in the overall spin multiplicity and hence relatively a larger barrier. For the  $^2\text{1}_{\text{hs-hs}}$  state, the hydrogen atom abstraction is found to occur in the  $\sigma$  channel while the rebound step is found to occur in the  $\pi$  channel. It is observed that the  $\text{Fe}^{\text{III}}-\text{O}(1)-\text{C}(1)$  angles of the  $\text{Ia}^{-2}\text{TS}_{\text{rebhs-hs}}$  ( $139^\circ$ ) are different from the  $\text{I}^{-2}\text{TS}_{\text{Hhs-hs}}$  ( $155^\circ$ ).<sup>160</sup> During the formation of the **I-Int**, both the  $\text{Fe}^{\text{III}}$  centres are exchange saturated, and hence higher spin states require additional pairing energy leading to relatively larger

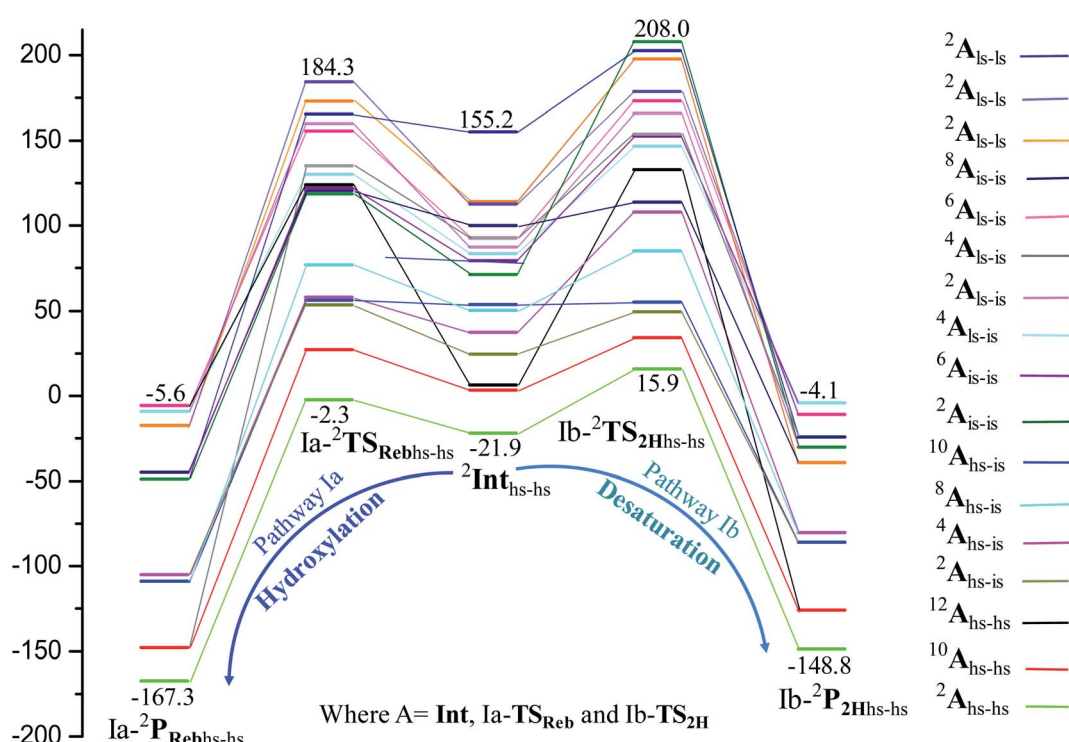


Fig. 7 B3LYP-D3 computed PES for the formation of  $\text{C}_5\text{H}_{11}\text{OH}/\text{C}_5\text{H}_{10}$  through intermediates leading to desaturation and hydroxylation (energies are in  $\text{kJ mol}^{-1}$ ).



barrier heights. At the doublet spin surface, however, both the spin-up and spin-down electrons are separated in a spin-polarised state offering flexibility in accepting either spin-down or spin-up electrons without compromising the overall spin multiplicity as shown in the electron-shift diagram in Fig. S19 in the ESI.<sup>†</sup> Thus, the antiferromagnetic coupling between the two Fe centres was found to be crucial in dictating the diverse reactivity observed. Furthermore, we have also computed all seventeen transition states corresponding to the second hydrogen atom abstraction of the cyclopentyl radical (pathway Ib) with **Ib-<sup>2</sup>TS<sub>2Hhs-hs</sub>** being found to have the lowest barrier height (37.8 kJ mol<sup>-1</sup>) followed by **Ib-<sup>12</sup>TS<sub>2Hhs-hs</sub>**, **Ib-<sup>10</sup>TS<sub>2Hhs-hs</sub>**, **Ib-<sup>2</sup>TS<sub>2Hhs-hs</sub>**, **Ib-<sup>10</sup>TS<sub>2Hhs-is</sub>**, **Ib-<sup>8</sup>TS<sub>2Hhs-is</sub>**, **Ib-<sup>4</sup>TS<sub>2Hhs-is</sub>**, **Ib-<sup>2</sup>TS<sub>2Hhs-is</sub>**, **Ib-<sup>8</sup>TS<sub>2Hhs-is</sub>**, **Ib-<sup>6</sup>TS<sub>2Hhs-is</sub>**, **Ib-<sup>2</sup>TS<sub>2Hhs-is</sub>**, **Ib-<sup>4</sup>TS<sub>2Hhs-is</sub>**, **Ib-<sup>2</sup>TS<sub>2Hhs-is</sub>**, **Ib-<sup>6</sup>TS<sub>2Hhs-is</sub>**, **Ib-<sup>4</sup>TS<sub>2Hhs-is</sub>**, **Ib-<sup>4</sup>TS<sub>2Hhs-is</sub>** and **Ib-<sup>2</sup>TS<sub>2Hhs-is</sub>** transitions states with a barrier height of 154.7, 56.1, 77.1, 107.1, 130.1, 71.3, 135.8, 174.6, 229.9, 224.7, 219.8, 200.7, 195.2, 175.6168.7 and 188.1 kJ mol<sup>-1</sup>, respectively. For the **Ib-<sup>2</sup>TS<sub>2Hhs-hs</sub>** transition state (see Fig. 8c and d), the Fe<sup>III</sup>–O(2)H bond is further elongated (1.940 Å) compared to the intermediate and the newly formed O(2)–H(2) and H(2)–C(2) bonds are 1.336 Å and 1.291 Å long respectively.

At the **Ib-<sup>2</sup>TS<sub>2Hhs-hs</sub>** state the O(2)–H(2)–C(2) (cyclopentyl radical) bond angle is determined to be 166° while the Fe<sup>III</sup>–O1–H1 angle is also determined to be 157°. The σ channel reactivity observed here is unusual compared to other systems and the presence of two Fe centres and significant electronic cooperativity that operates between them facilitate such behaviour.

A closer look at the orbital diagram and orbital occupation reveals an interesting picture wherein at the **Ib-<sup>2</sup>TS<sub>2Hhs-hs</sub>** transition state, an  $\alpha$  electron from C2–H gets transferred to the  $\sigma^*(d_{z^2})$  of the Fe<sup>III</sup> ( $S_a$ ) iron centre, and at the same time, it has lost another  $\alpha$  electron to the second Fe<sup>III</sup> ( $S_b$ ) centre, *i.e.* an electron transfer from the substrate triggers a simultaneous internal electron transfer from one Fe<sup>III</sup> centre to the second Fe centre revealing the presence of electronic cooperativity between the two Fe<sup>III</sup> centres. We have witnessed such electronic cooperativity earlier in dinuclear iron(IV)–oxo<sup>90</sup> and iron(IV)–oxo–nitrido species<sup>71</sup> and detecting a similar scenario here in the mixed-valence iron(III/IV) dimer reveals a similar pattern among dinuclear complexes. After transferring an electron from the cyclopentyl radical, the  $S_a$  remains as the Fe<sup>III</sup>–O(2)H group while  $S_b$  becomes an Fe<sup>II</sup>–O(1)H(1) centre (see Fig. 3d and S20 in the ESI<sup>†</sup>).

In pathway Ia, the –OH group is expected to rebound to the cyclopentyl radical to give cyclopentanol (**Ia-P<sub>reb</sub>**). Here, we have computed eight possible spin states with **Ia-<sup>10</sup>P<sub>rebhs-hs</sub>** lying at -147.8 kJ mol<sup>-1</sup> (from the <sup>2</sup>1<sub>hs-hs</sub> state, see ESI<sup>†</sup> for other energies). The thermodynamic formation of this product is estimated to be -167.3 kJ mol<sup>-1</sup>, indicating the facile formation of this product. In the <sup>2</sup>P<sub>rebhs-hs</sub> state, both the iron centres are antiferromagnetically coupled with the coupling constant ( $J$ ) being -150.5 cm<sup>-1</sup> (see Fig. 8e and f for the optimised structure, and for the spin density plot of SNOs see Fig. S21 in the ESI<sup>†</sup>). In pathway Ib, the terminal –O(2)H group is expected to abstract a second hydrogen atom from the cyclopentyl radical to give cyclopentene (**Ib-<sup>2</sup>P<sub>2Hhs-hs</sub>** lying at -148.8 kJ mol<sup>-1</sup> with a  $J$

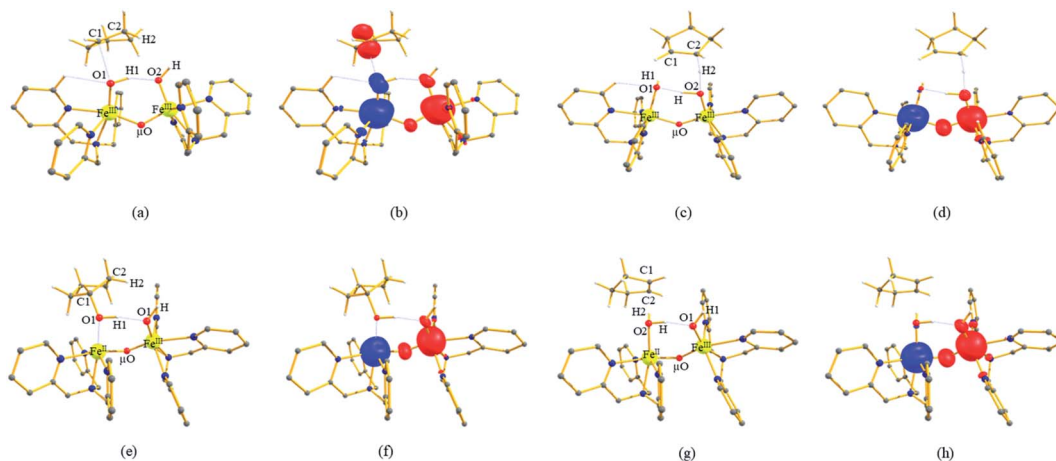


**Fig. 8** (a and b) The optimized structure of **Ia-<sup>2</sup>TS<sub>rebhs-hs</sub>** and its corresponding spin density plot, (c and d) optimized structure of **Ib-<sup>2</sup>TS<sub>2Hhs-hs</sub>** and its corresponding spin density plot, (e and f) the optimized structure of **Ia-<sup>2</sup>P<sub>rebhs-hs</sub>** and its corresponding spin density plot, and (g and h) the optimized structure of **Ib-<sup>2</sup>P<sub>2Hhs-hs</sub>** and its corresponding spin density plot. Some important structural parameters computed for the spin states and spin density values are given below for species **Ia-TS<sub>reb</sub>**, **Ib-TS<sub>2H</sub>**, **Ia-<sup>2</sup>P<sub>rebhs-hs</sub>** and **Ib-<sup>2</sup>P<sub>2Hhs-hs</sub>**. For spin state **Ia-<sup>2</sup>TS<sub>rebhs-hs</sub>**, Fe<sup>III</sup>–O1 = 1.851, Fe<sup>III</sup>–O2 = 1.889, Fe<sup>III</sup>–μO = 1.852, Fe<sup>III</sup>–μO1 = 1.784, O1–H1 = 0.986, O1–C1 = 2.649,  $\angle$  Fe<sup>III</sup>–O1–C1 = 139°, and  $\angle$  H1–O1–C1 = 82° and spin density Fe<sup>III</sup> = -3.92, Fe<sup>III</sup> = 3.96, O1 = -0.37, O2 = 0.23, μO = 0.21, C1 = 0.85. For spin state **Ib-<sup>2</sup>TS<sub>2Hhs-hs</sub>**, Fe<sup>III</sup>–O1 = 2.111, Fe<sup>III</sup>–O2 = 1.940, Fe<sup>III</sup>–μO = 1.899, Fe<sup>III</sup>–μO1 = 1.770, O2–H2 = 1.336, H2–C2 = 1.291,  $\angle$  Fe<sup>III</sup>–O1–H1 = 157°, and  $\angle$  O1–H1–C1 = 166° and spin density Fe<sup>III</sup> = -3.64, Fe<sup>III</sup> = 3.94, O1 = -0.02, O2 = 0.14, μO = 0.42, and C2 = -0.02. For spin state **Ia-<sup>2</sup>P<sub>rebhs-hs</sub>**, Fe<sup>II</sup>–O1 = 2.158, Fe<sup>III</sup>–O2 = 1.923, Fe<sup>II</sup>–μO = 1.876, Fe<sup>III</sup>–μO = 1.769, O1–H1 = 1.010, O1–C1 = 1.444,  $\angle$  Fe<sup>II</sup>–O1–C1 = 101°, and  $\angle$  H1–O1–C1 = 110° and spin density Fe<sup>II</sup> = -3.66, Fe<sup>III</sup> = 3.96, O1 = -0.02, O2 = 0.18, μO = 0.41, and C1 = 0.00. For spin state **Ib-<sup>2</sup>P<sub>2Hhs-hs</sub>**, Fe<sup>III</sup>–O1 = 1.928, Fe<sup>II</sup>–O2 = 2.163, Fe<sup>III</sup>–μO = 1.769, Fe<sup>II</sup>–μO = 1.879, O2–H2 = 0.977, H2–C2 = 3.059,  $\angle$  Fe<sup>II</sup>–O2–H2 = 114°, and  $\angle$  O2–H2–C2 = 147° and spin density Fe<sup>III</sup> = 3.95, Fe<sup>II</sup> = -3.64, O1 = -0.03, O2 = 0.18, μO = 0.41, and C2 = 0.00. All bond lengths are given in Å and angles are given in °. All hydrogen atoms (except O2–H, C1–H1 and C2–H2) are omitted for clarity.



value of  $-141.4\text{ cm}^{-1}$ , see Fig. 8g and h and S22 for SNOs in the ESI†). Additional calculations performed incorporating counterions reveal that relative energies of the doublet and dectet pathways are not altered significantly (see Fig. S23 in the ESI†).

In pathway Ic, the  $\mu$ -oxo atom abstracts a second hydrogen atom from the cyclopentyl radical (**I-Int1**) to produce cyclopentene (**Ic-P<sub>2H</sub>**) via **Ic-TS<sub>2H</sub>** (see Scheme 2 and Fig. S24 in the ESI†). The calculated barrier height is found to be  $54.7\text{ kJ mol}^{-1}$  at the doublet surface. This clearly suggests that pathway Ic is less favourable compared to Ib and this is likely due to the accessibility of the bridged oxygen atom and the constraint that it imposed on the substrate compared to the terminal metal-oxo species. In pathway II, the  $\{\text{O}\text{Fe}^{\text{III}}-\mu(\text{OH})-\text{Fe}^{\text{III}}(\text{OH})\}$  intermediate species is expected to rebound with the cyclopentyl radical to produce cyclopentanol, and this is found to have a prohibitively high barrier ( $189.6\text{ kJ mol}^{-1}$  at the doublet surface for **II-<sup>2</sup>TS<sub>reb</sub>**) suggesting that the hydroxylation is unlikely to proceed via the  $\mu\text{-O}/\mu\text{-OH}$  bridges. The formation of cyclopentanol is also found to be energetically less favoured compared to pathway Ia (see Fig. 6). In pathway III, the second hydrogen atom abstraction from the cyclopentyl radical via the transition state (**III-<sup>2</sup>TS<sub>2H</sub>**) is expected to yield a desaturated product. Here the estimated barrier is  $9.0\text{ kJ mol}^{-1}$  from the preceding intermediate **III-<sup>2</sup>Int**, which is strongly destabilised (endothermic compared to the reactant) leading to a desaturated product. Our computed energetics reveal that both pathways II and III are energetically demanding (compared to pathway I), and hence the reaction is unlikely to proceed through these pathways (see Fig. 6).

## Discussion

While orbital selection rules for the choice of hydroxylation *vs.* desaturation are clear for mononuclear  $\text{Fe}^{\text{IV}}=\text{O}$  groups,<sup>66,159</sup> for dinuclear species these are not established. Several experimental reports claim robust reactivity for dinuclear metal-oxo species compared to the monomeric one, and this has high-relevance to the very high reactivity reported for sMMO enzymes possessing dinuclear Fe centres. Generally, for mononuclear iron(IV)-oxo species, hydroxylation has been observed for many catalysts (with the substrate which are not specifically biased towards desaturation) while this is a rare feat in diiron(IV)-oxo chemistry. A terminal  $\text{Fe}^{\text{III}}-\text{OH}$  formed with mononuclear complexes tends to rebound with the radical as they are poor electrophiles to abstract another hydrogen atom from the mono-radical species produced. In the case of dinuclear iron(IV)-oxo species, the intermediate generated is  $\{\text{Fe}^{\text{III}}-\mu(\text{OH})-\text{Fe}^{\text{IV}}\}$  or  $\{\text{Fe}^{\text{III}}-\mu(\text{OH})\mu(\text{O})-\text{Fe}^{\text{IV}}\}$  species where the  $-\text{OH}$  groups are bridged between two Fe centres. This raises the rebound barriers significantly as the  $\mu\text{-OH}$  bridge is not in a favorable orientation to have a greater overlap with the radical SOMOs to generate the desired hydroxylated product. To form hydroxylation products, significant distortion at the coordination sphere is required, and this adds a significant energy penalty to the rebound barriers. Additionally, once the first hydrogen atom is abstracted by the diiron(IV)-oxo group, this results in  $\{\text{Fe}^{\text{III}}-\mu(\text{OH})-\text{Fe}^{\text{IV}}\}$  type species, and here the  $-\text{OH}$

groups are still bonded to one of the  $\text{Fe}^{\text{IV}}$  centres and are thus not necessarily poor electrophiles to abstract the second hydrogen atom from the substrate. Therefore, these species tend to form desaturation rather than hydroxylation. However, the scenario is very different for the  $[\text{HO}(\text{L})\text{Fe}^{\text{III}}-\text{O}-\text{Fe}^{\text{IV}}(\text{O})(\text{L})]^{2+}$  active complex that has been reported to perform both hydroxylation as well as desaturation.<sup>8</sup> Here we intend to understand the mechanistic pathway by which this complex performs both activities at ease. The first hydrogen atom abstraction has been assumed to take place by terminal  $\text{Fe}^{\text{IV}}=\text{O}(1)$  species which has the lowest barrier among all ( $38.3\text{ kJ mol}^{-1}$  at the antiferromagnetically coupled doublet surface but merely  $20.2\text{ kJ mol}^{-1}$  from the reactant) followed by the terminal  $\text{Fe}^{\text{III}}-\text{O}(2)\text{H}$  species ( $126.2\text{ kJ mol}^{-1}$  at the doublet surface) and  $\mu$ -oxo bridged oxygen ( $160.1\text{ kJ mol}^{-1}$  at the doublet surface). Clearly, calculations reveal that the first hydrogen atom abstraction is triggered here by the terminal  $\text{Fe}^{\text{IV}}=\text{O}(1)$  as the other two possible centres are much poorer electrophiles. The million-fold reactivity that is observed essentially stems from the fact that the first hydrogen atom abstraction, which is the rate-determining step here, is found to be extremely small with this complex. To analyse and understand this particular feature, we have compared the barrier height for C-H bond activation by this complex for DHA (where DHA = 9,10-dihydroanthracene and this substrate is more common in the literature) with available di and mononuclear  $\text{Fe}^{\text{IV}}=\text{O}$  species and found that the barriers are extremely small and in fact, they are three times smaller than Cpd I models estimated (see Table S10 in the ESI†).<sup>161</sup>

We have further probed the electronic origin of this lower barrier wherein the empty  $\beta-\sigma_{z^2}^*$  of the  $\text{Fe}^{\text{IV}}$  centre is important as it accepts electrons during the course of reactivity. This orbital is found to strongly mix with the  $\pi_{xz}^*$  orbital of the  $\text{Fe}^{\text{III}}$  centre (see Fig. 9a). Such orbital mixing sometimes called as cross-interaction has been known in dinuclear complexes for some time.<sup>162</sup> Further at the transition state as well, the  $\sigma_{z^2}^*-\pi_{xz}^*$  overlap is visible, reducing the antibonding interactions between the metal d-orbital and the ligand at the HOMO (see Fig. 9b) offering a spin-cooperation between the two centres. Additionally, the ferryl-bent which has been mentioned earlier, also a reason for the lowering of the  $\sigma_{z^2}^*-\pi_{xz}^*$  orbital as the bent seen in **1** is much larger than the largest ferryl-bent reported in mononuclear complexes.<sup>140,141</sup> Additional analysis performed in the  $\text{Co}^{\text{III}}/\text{Ga}^{\text{III}}$  fictitious model reveals stabilisation of  $\sigma_{z^2}^*$  in the presence of  $\text{Fe}^{\text{III}}$  ions (see Fig. S25 in the ESI†).

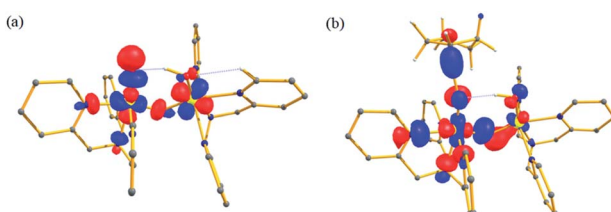


Fig. 9 Computed orbital diagram corresponding to the (a) LUMO of the  ${}^2\text{I}_{\text{hs-hs}}$  and (b) HOMO of the  $\text{I-}{}^2\text{TS}_{\text{Hhs-hs}}$ .



To further understand the origin of the differences among different pathways studied, we carefully looked into the frontier orbitals. The orientation of frontier orbitals offers clues on the flexibility available for the substrate for its reactivity. In the terminal  $\text{Fe}^{\text{IV}}=\text{O}$  bond, the  $\sigma^*$   $d_{z^2}$  orbital is found to be high lying in energy compared with the other four orbitals of the iron centre. This triggers the lower energy  $\sigma$ -pathway for the hydrogen atom abstraction. Further, the energy gap between the acceptor and donor orbitals gives some clues on the reactivity pattern as has been demonstrated for other  $\text{Fe}^{\text{IV}}=\text{O}$  species.<sup>163</sup> We have calculated the energy difference between the LUMO of the  $\text{Fe}=\text{O}$   $\sigma^*$  and  $\sigma_{\text{CH}}$  orbitals of the adjacent C–H bond of cyclopentane to be 1.09 eV for the  $^2\text{1}_{\text{hs-hs}}$  spin state, while for the  $^{10}\text{1}_{\text{hs-hs}}$  spin state it is found to be 1.35 eV in the gas phase. These HOMO–LUMO gaps suggest that the  $^2\text{1}_{\text{hs-hs}}$  spin state is more reactive towards C–H activation of cyclopentane than the  $^{10}\text{1}_{\text{hs-hs}}$  spin state. These two values are comparable with the earlier reported model complexes for methane and cyclohexane as a substrate.<sup>90,163</sup> If a similar analysis is carried out assuming terminal  $\text{Fe}^{\text{III}}-\text{O}(2)\text{H}$  or the bridged  $\mu$ -oxo as the electrophile, it can be found that the energy gap between those frontier molecular orbitals (FMO) is 3.72 and 4.64 eV, respectively. These are much higher than that of the terminal  $\text{Fe}^{\text{IV}}=\text{O}$  species, revealing the origin of sluggish reactivity for these electrophilic groups present in **1**. Additionally, the position of the substrate also adds a significant energy penalty as the linear  $\sigma$  pathway is not found for both pathways II and III. Likewise, we have calculated the energy gap between the LUMO of the  $\text{Co}^{\text{III}}/\text{Ga}^{\text{III}}$  fictitious model and FMO of the targeted  $\sigma_{\text{CH}}$  of the cyclopentane. The gap is found to be 1.69/1.62 eV, suggesting a higher reactivity for species **1** towards cyclopentane than both the  $\text{Co}^{\text{III}}/\text{Ga}^{\text{III}}$  fictitious models.

To assess further, deformation energies for the corresponding transition states are computed, and these are estimated to be 29.9, 118.1, and 71.9 kJ mol<sup>-1</sup> for **I**<sup>2</sup> $\text{TS}_{\text{Hhs-hs}}$ , **II**<sup>2</sup> $\text{TS}_{\text{Hhs-hs}}$ , and **III**<sup>2</sup> $\text{TS}_{\text{Hhs-hs}}$ , respectively. The deformation energy at the transition state contributes 78% to the barrier height in pathway I, while in pathways II and III, these were estimated to be 74 and 57%, respectively. Interestingly, while deformation is the major contributor for pathways I and II, in pathway III, other contributions dominate the barrier height. A closer look at the interaction energy reveals that in pathway III the interaction energy is very significant compared to pathways I and II. This may be attributed to the fact that the  $\text{Fe}^{\text{III}}-\text{OH}$  centre is already exchange saturated (see Table S11 in the ESI†).

To further understand the structural origin of the effects that are observed, we have also plotted the structure overlay of **I**<sup>2</sup> $\text{RC}_{\text{hs-hs}}$ , **I**<sup>2</sup> $\text{TS}_{\text{Hhs-hs}}$ , **II**<sup>2</sup> $\text{TS}_{\text{Hhs-hs}}$ , and **III**<sup>2</sup> $\text{TS}_{\text{Hhs-hs}}$  (see Fig. 10). This overlay structure reveals that the **I**<sup>2</sup> $\text{TS}_{\text{Hhs-hs}}$  deviated the least from the **I**<sup>2</sup> $\text{RC}_{\text{hs-hs}}$  compared to other two transition states (RMSD for the complex (cyclopentane) 0.38 (0.21) compared to 3.13 (0.58) and 1.28 (0.18) Å for **II**<sup>2</sup> $\text{TS}_{\text{Hhs-hs}}$  and **III**<sup>2</sup> $\text{TS}_{\text{Hhs-hs}}$ , respectively) and hence required very low reorganisation energy. This could be due to the preference for the  $\sigma$  pathway, which attempts to keep the substrate slightly further from the ligand moiety compared to the  $\pi$  pathway that is observed for the other two transition states.

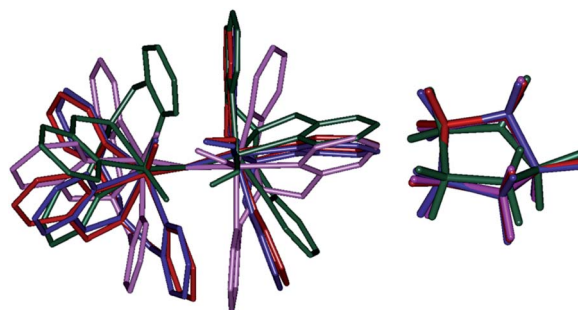


Fig. 10 Structural overlay of  $^2\text{RC}_{\text{hs-hs}}$  (blue), **I**<sup>2</sup> $\text{TS}_{\text{Hhs-hs}}$  (red), **II**<sup>2</sup> $\text{TS}_{\text{Hhs-hs}}$  (dark green), and **III**<sup>2</sup> $\text{TS}_{\text{Hhs-hs}}$  (magenta) and their corresponding cyclopentane ring (right) shown separately. H atoms are omitted for clarity.

Further, we have also estimated the  $\text{BDE}_{\text{OH}}/\text{D}_{\text{CH}}$  values<sup>5,72,164–171</sup> for the three different pathways we described and our calculated  $\text{BDE}_{\text{O1H1}}/\text{D}_{\text{C1H1}}$  values for the **I**<sup>2</sup> $\text{Int}_{\text{hs-hs}}$ , **II**<sup>2</sup> $\text{Int}_{\text{hs-hs}}$ , and **III**<sup>2</sup> $\text{Int}_{\text{hs-hs}}$  are 382.0/388.6, 311.0/390.7 and 284.6/389.0 kJ mol<sup>-1</sup> (see the Thermochemistry section for equations eqn (1)–(3) in the ESI† for details). These values suggest that the terminal  $\text{Fe}^{\text{IV}}=\text{O}$  species is a much better oxidant than either terminal  $\text{Fe}^{\text{III}}-\text{OH}$  or bridged  $\mu$ -oxo for hydroxylation as well as desaturation reactions. Therefore, the terminal  $\text{Fe}^{\text{IV}}=\text{O}$  species is found to be a more powerful oxidant of hydrogen atom transfer from cyclopentane than  $\text{Fe}^{\text{III}}-\text{OH}$  or bridged  $\mu$ -oxo due to the increased basicity of the iron–hydroxo species that is formed. This is mainly due to the presence of orbital reorganisation that affects the electron affinity of the oxidant. Besides, we have carefully analysed bond parameters of the bond breaking of the C–H bond to the transition state structure from the reactant complex as well as the O–H bond formation of the intermediate species from the corresponding transition state structure.<sup>164</sup> These two parameters (%  $\text{BB}_{\text{CH}}$  and %  $\text{BF}_{\text{OH}}$ ) are generally correlated with an activation energy of the C–H bond during hydrogen atom abstraction (see Table S12 in the ESI†). Depending on whether a transition state is reactant-like or product-like, one can relate this to the estimated barrier height. By comparing the bond parameters, the **I**<sup>2</sup> $\text{TS}_{\text{Hhs-hs}}$  transition state is found to be an early transition state compared to **II**<sup>2</sup> $\text{TS}_{\text{Hhs-hs}}$  and **III**<sup>2</sup> $\text{TS}_{\text{Hhs-hs}}$  (see Fig. S26 and S27 in the ESI†). This also supports the energetics computed.<sup>164</sup>

Further, we have analysed the corresponding transition state for the hydroxylation (**Ia**<sup>2</sup> $\text{TS}_{\text{rebhs-hs}}$ ) and second hydrogen atom abstraction (**Ib**<sup>2</sup> $\text{TS}_{\text{2Hhs-hs}}$ ) reaction, to assess why rebound is slightly preferred over second hydrogen atom abstraction for species **1**. The computed lower bound barrier for  $-\text{OH}$  rebound from  $\text{Fe}^{\text{III}}-\text{O}(1)\text{H}(1)$  species is 19.6 kJ mol<sup>-1</sup> while for second hydrogen abstraction from the  $\text{Fe}^{\text{III}}-\text{O}(2)\text{H}$  is estimated to be 37.9 kJ mol<sup>-1</sup> with respect to the **I**<sup>2</sup> $\text{Int}_{\text{hs-hs}}$  species. In the case of the second hydrogen abstraction, the barrier is higher, which is correlated with the approach of the cyclopentyl radical towards the hydroxyl group, and the total deformation energy is computed to be 50.5 kJ mol<sup>-1</sup> for the **Ib**<sup>2</sup> $\text{TS}_{\text{2Hhs-hs}}$  species. As the barrier computed is 37.9 kJ mol<sup>-1</sup>, the difference of 12.6 kJ mol<sup>-1</sup> is due to the electronic contribution to the



transition state. The deformation energy computed for the  $-\text{OH}$  rebound transition state is much lower (23.9 kJ mol<sup>-1</sup> see Fig. S28 in the ESI<sup>†</sup>). Here, electronic contribution dominates over the steric effect, *i.e.*, the observed barrier heights are lower than the deformation energy of the transition state. Additionally, a very large dipole moment of 13.0 D for **Ia-<sup>2</sup>TS<sub>rebhs-hs</sub>** species was estimated, while rather a smaller dipole moment was detected (4.6 D) for the **Ib-<sup>2</sup>TS<sub>2Hhs-hs</sub>** species. We have also estimated the percentages of interaction/bond formation between O(1)/O(2) and C(1)/H(2) atoms for the formation of the product and it was found that the rebound transition state is a relatively early transition state compared to second hydrogen atom abstraction reflecting the estimated barrier heights (see Table S13 in the ESI<sup>†</sup>).

Further, we have attempted to understand the selectivity of the reaction mechanism with the help of the valence bond (VB) curve-crossing diagram (see Fig. 11). These types of VB diagrams were used previously to explain the electronic level selectivity of rebound and second hydrogen abstraction pathway.<sup>164,165,172-174</sup> In the entire discussion of this section, we have considered only those used previously to explain the electronic level selectivity of the thermodynamically low-lying doublet state intermediate (**I-<sup>2</sup>Int**). In reactant **1**, the iron-oxo centre ( $S_b$ ) has four spin-down electrons with the Fe<sup>IV</sup> state and the iron-hydroxo centre ( $S_a$ ) has five up-spin electrons with the Fe<sup>III</sup> state. The combined effect of EET and antiferromagnetically coupled stabilisation leads to the C-H activation of cyclopentane through **Ib-<sup>2</sup>TS<sub>Hhs-hs</sub>**, and this has been discussed elaborately in previous sections. The transition state leads to the hydroxylated intermediate (**I-<sup>2</sup>Int**), and in this intermediate, both iron centres ( $S_a$  and  $S_b$ ) have a similar electronic occupation in the core orbital and difference in spin orientation. In the VBT diagram, we have demonstrated the pathway electronic

level selectivity of the hydroxylation product *via* **Ia-<sup>2</sup>TS<sub>rebhs-hs</sub>** and the second hydrogen abstraction product *via* the **Ib-<sup>2</sup>TS<sub>2H-</sub>hs-hs** transition state (see Fig. S13 in the ESI<sup>†</sup>).

The mechanistic features and electronic cooperativity that is observed during the course of reactions are captured well by the valence bond curve crossing diagram. In valence bond theory, the ground state wave function has been represented as  $\psi$ , and its corresponding excited state wave function has been represented as  $\psi^*$ . Here, the intermediate wave function ( $\psi_i$ ) has been considered as a hypothetical reactant part ( $\psi_r$ ), and the product wave function is denoted as  $\psi_p$ . The electronic configuration changes of both  $S_b$  and  $S_a$  centres in **Ib-<sup>2</sup>TS<sub>2Hhs-hs</sub>** and **Ia-<sup>2</sup>TS<sub>rebhs-hs</sub>** have been discussed for getting clarity on the higher selectivity of hydroxylation over second hydrogen abstraction. The energy barrier height from the intermediate to the product is directly proportional to the excitation energy from  $\psi_r$  to  $\psi_p$ .<sup>175</sup> The comparison of the VB structure of both products from intermediate configurations gives qualitative insights into the chemical and physical components of the transition state. In the case of **Ia-<sup>2</sup>TS<sub>rebhs-hs</sub>**, the association of the spin-up electron  $\phi(C1)$  of the substrate with the  $2p_z(O)$  orbital of the hydroxyl bond and the  $(\sigma_{z^2}^*)^1$  orbital of the  $S_b$  centre in the intermediate ( $\psi_r$ ) alters the overall MO picture. The core orbital occupation configuration changes from  $(\delta_{xy})^1$ ,  $(\pi_{xz}^*)^1$ ,  $(\pi_{yz}^*)^1$ ,  $(\sigma_{x^2-y^2}^*)^1$ , and  $(\sigma_{z^2}^*)^1$  to  $(\delta_{xy})^1$ ,  $(\pi_{xz}^*)^1$ ,  $(\pi_{yz}^*)^1$ ,  $(\sigma_{x^2-y^2}^*)^1$ , and  $(\sigma_{z^2}^*)^1$  and the activation energy simply depends on the electron association steps. The promotion gap ( $G_{\text{reb}}$ ) of **Ia-<sup>2</sup>TS<sub>rebhs-hs</sub>** depends on the ionisation potential of the substrate (IE<sub>Alk</sub>), the electron affinity of the acceptor part on the intermediate (EA<sub>Fe<sup>III</sup>-OH</sub>) and the energy of the intermediate with changes in their molecular orbital energies,

$$G_{\text{reb}} = \text{IE}_{\text{Alk}} - \text{EA}_{\text{Fe}^{(\text{III})}-\text{OH}} + E_{\text{Fe}^{(\text{III})}-\text{OH}} + E_{\text{MO}}$$

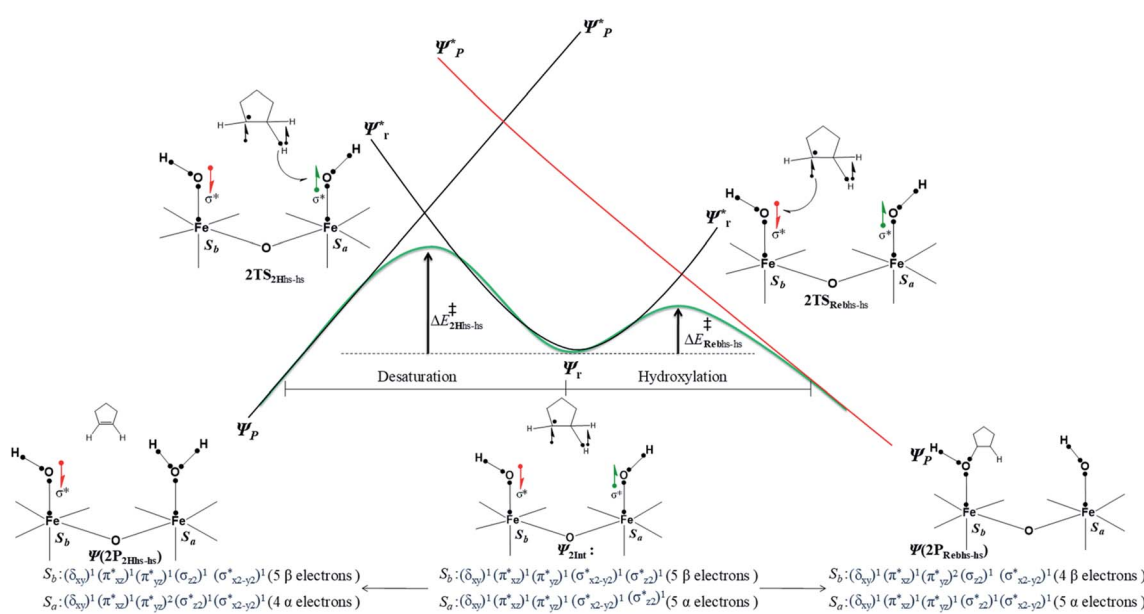


Fig. 11 Valence bond curve crossing diagram for the rebound transition state (**2TS<sub>rebhs-hs</sub>**) (a) and second hydrogen abstraction transition state (**2TS<sub>2Hhs-hs</sub>**) (b) from **2Int<sub>hs-hs</sub>**. Dots represent valence electrons, and lines implicate chemical bonds.



In the case of **Ib**<sup>2</sup>**TS**<sub>2H<sub>hs</sub>-hs</sub>, the second hydrogen abstraction barrier is determined by the energy of the  $\sigma_{\text{CH}}$  bond of the intermediate that is broken into atomic orbitals ( $E_{\sigma(\text{C-H})}$ ). In addition, it is based on the energy of the acceptor intermediate ( $E_{\text{Fe}(\text{III})-\text{OH}}$ ). Apart from that, the energy barrier height also depends on molecular orbital changes with electronic reorganisation energy within the orbital because of the need of internal electron flipping for effective product formation. The dissociated hydrogen radical with the 1s(H) orbital is combined with the 2p<sub>z</sub>(O) orbital of hydroxyl oxygen, and the core orbital electronic configuration changes from  $(\delta_{xy})^1$ ,  $(\pi_{xz}^*)^1$ ,  $(\pi_{yz}^*)^1$ ,  $(\sigma_{x^2-y^2}^*)^1$ , and  $(\sigma_{z^2}^*)^1$  to  $(\delta_{xy})^1$ ,  $(\pi_{xz}^*)^1$ ,  $(\pi_{yz}^*)^2$ ,  $(\sigma_{x^2-y^2}^*)^1$ , and  $(\sigma_{z^2}^*)^1$  at the S<sub>a</sub> iron centre. Hence the promotion gap ( $G_{2\text{H}}$ ) will be the sum of ( $E_{\sigma(\text{C-H})}$ ) dissociation, the energy of the substrate ( $E_{\text{Fe}(\text{III})-\text{OH}}$ ), and molecular orbital changes for electronic reorganisation with electron flipping.

$$G_{2\text{H}} = E_{\sigma(\text{C-H})} - E_{\text{Fe}(\text{III})-\text{OH}} + E_{\text{MO}} \text{ (both molecular orbital changes and electron flipping from spin-up to spin-down)}$$

Thus, for these reasons, **Ia**<sup>2</sup>**TS**<sub>rebhs-hs</sub> will have a smaller  $E_{\text{MO}}$  and promotion gap for excitation than the **Ib**<sup>2</sup>**TS**<sub>2H<sub>hs</sub>-hs</sub>. The small excitation energy, as well as higher reactivity of the **Ia**<sup>2</sup>**TS**<sub>rebhs-hs</sub> transition state was clearly demonstrated by the VBT curve crossing diagram.

## Conclusions

The conclusion derived from this work is summarized below

(i) Calculations support the experimental observation of the doublet ground state for  $[\text{HO}(\text{L})\text{Fe}^{\text{III}}-\text{O}-\text{Fe}^{\text{IV}}(\text{O})(\text{L})]^{2+}$  and various factors such as ferryl-bent and the weaker ligand field offered by the  $\mu$ -oxo group contribute to the unusual stabilisation of the high-spin terminal  $\text{Fe}^{\text{IV}}=\text{O}$  group. In  $[\text{HO}(\text{L})\text{Fe}^{\text{III}}-\text{O}-\text{Fe}^{\text{IV}}(\text{O})(\text{L})]^{2+}$  species there are three different electrophilic oxygen atoms that can abstract a hydrogen atom from the substrate. Our calculations suggest that the terminal  $\text{Fe}^{\text{IV}}=\text{O}$  (pathway I) is very aggressive as the barrier height computed is very small (20.2 kJ mol<sup>-1</sup> from the reactant) compared to  $\mu$ -oxo/terminal  $\text{Fe}^{\text{III}}-\text{OH}$  (pathway II/III) species which have 6–8 times higher barrier heights. This is essentially due to steric effects in the case of the  $\mu$ -oxo bridge and electronic effects in the case of  $\text{Fe}^{\text{III}}-\text{OH}$  species.

(ii) A million-fold reactivity observed for this species essentially stems from the extremely low first hydrogen atom abstraction barrier compared to several other mono/dinuclear iron-oxo species. The lower barrier observed here is attributed to various factors such as spin-cooperation, significant ferryl bending, and favourable  $\text{Fe}^{\text{IV}}\sigma_{z^2}^*|\text{Fe}^{\text{III}}\pi_{xz}^*$  overlap.

(iii) After the abstraction of the first hydrogen atom, the reaction is expected to proceed *via* either –OH rebound or abstraction of the second hydrogen atom leading to desaturation. Our calculations rule out –OH rebound/desaturation from the  $\mu$ -OH group (pathway II/Ic) or desaturation by the terminal  $\text{Fe}^{\text{III}}-\text{OH}$  species (pathway III) and suggest that either –OH

rebound from the terminal  $\text{Fe}^{\text{III}}-\text{OH}$  (pathway Ia with a barrier height of 19.6 kJ mol<sup>-1</sup>) or desaturation by the terminal  $\text{Fe}^{\text{III}}-\text{OH}$  is favourable (barrier height 37.8 kJ mol<sup>-1</sup> pathway Ib). A closer look at the electronic structure reveals an internal electron transfer from one Fe centre to the other during the second hydrogen atom abstraction that lowers the barrier height significantly. As such spin-cooperation is not possible in mononuclear complexes, they prefer to perform hydroxylation over desaturation for unbiased substrates and this substantiates the origin of the dual catalytic abilities that are observed for the  $[\text{HO}(\text{L})\text{Fe}^{\text{III}}-\text{O}-\text{Fe}^{\text{IV}}(\text{O})(\text{L})]^{2+}$  species.

To this end, here we have described in detail the electronic structure of the  $[\text{HO}(\text{L})\text{Fe}^{\text{III}}-\text{O}-\text{Fe}^{\text{IV}}(\text{O})(\text{L})]^{2+}$  species and probed its origin of very high-reactivity observed compared to other mono/dinuclear oxo species. Our results unequivocally reveal the importance of spin-states, spin-coupling, and cooperation of spin moments between the two centres that control the reactivity and product selectivity. The conception of the open core being more reactive compared to a diamond-core motif in diiron-oxo chemistry has far-reaching consequences as the nature of the active catalyst at the sMMO enzyme is elusive. Substitution of the –OH group with other groups was found to influence the reactivity significantly, and our group is currently working on this aspect, which will be reported in future.

## Conflicts of interest

There are no conflicts to declare.

## Acknowledgements

G. R. would like to acknowledge the financial support from DST and SERB (DST/SJF/CAS-03/2018–19; CRG/2018/000430) India, and IIT Bombay for the high-performance computing facility. D. S. thanks SERB, India for the award of Core Research Grant (EMR/2017/000745) and Prof. S. Shaik (Hebrew University of Jerusalem) for his help and comments. M. A. would like to thank IIT Bombay for financial support.

## Notes and references

- 1 M. A. Ehudin, D. A. Quist and K. D. Karlin, *J. Am. Chem. Soc.*, 2019, **141**, 12558–12569.
- 2 S. Kal, A. Draksharapu and L. Que Jr, *J. Am. Chem. Soc.*, 2018, **140**, 5798–5804.
- 3 M. A. Ehudin, L. B. Gee, S. Sabuncu, A. Braun, P. Moënne-Locoz, B. Hedman, K. O. Hodgson, E. I. Solomon and K. D. Karlin, *J. Am. Chem. Soc.*, 2019, **141**, 5942–5960.
- 4 S. Ghafoor, A. Mansha and S. P. de Visser, *J. Am. Chem. Soc.*, 2019, **141**, 20278–20292.
- 5 K. Mittra and M. T. Green, *J. Am. Chem. Soc.*, 2019, **141**, 5504–5510.
- 6 T. H. Yosca, M. C. Langston, C. M. Krest, E. L. Onderko, T. L. Grove, J. Livada and M. T. Green, *J. Am. Chem. Soc.*, 2016, **138**, 16016–16023.
- 7 G. Xue, A. T. Fiedler, M. Martinho, E. Münck and L. Que, *Proc. Natl. Acad. Sci. U. S. A.*, 2008, **105**, 20615–20620.



8 G. Xue, R. De Hont, E. Münck and L. Que Jr, *Nat. Chem.*, 2010, **2**, 400–405.

9 G. Xue, D. Wang, R. De Hont, A. T. Fiedler, X. Shan, E. Münck and L. Que, *Proc. Natl. Acad. Sci. U. S. A.*, 2007, **104**, 20713–20718.

10 G. Xue, A. Pokutsa and L. Que Jr, *J. Am. Chem. Soc.*, 2011, **133**, 16657–16667.

11 C. Kim, Y. Dong and L. Que, *J. Am. Chem. Soc.*, 1997, **119**, 3635–3636.

12 A. Ghosh, F. Tiago de Oliveira, T. Yano, T. Nishioka, E. S. Beach, I. Kinoshita, E. Münck, A. D. Ryabov, C. P. Horwitz and T. J. Collins, *J. Am. Chem. Soc.*, 2005, **127**, 2505–2513.

13 G. E. Cutsail III, R. Banerjee, A. Zhou, L. Que Jr, J. D. Lipscomb and S. DeBeer, *J. Am. Chem. Soc.*, 2018, **140**, 16807–16820.

14 G. Capocasa, F. Sessa, F. Tavani, M. Monte, G. Olivo, S. Pasquarelli, O. Lanzalunga, S. Di Stefano and P. D'Angelo, *J. Am. Chem. Soc.*, 2019, **141**, 2299–2304.

15 P. Verma, K. D. Vogiatzis, N. Planas, J. Borycz, D. J. Xiao, J. R. Long, L. Gagliardi and D. G. Truhlar, *J. Am. Chem. Soc.*, 2015, **137**, 5770–5781.

16 S. Sahu and D. P. Goldberg, *J. Am. Chem. Soc.*, 2016, **138**, 11410–11428.

17 R. Fan, J. Serrano-Plana, W. N. Oloo, A. Draksharapu, E. Delgado-Pinar, A. Company, V. Martin-Diaconescu, M. Borrell, J. Lloret-Fillol and E. Garcia-Espana, *J. Am. Chem. Soc.*, 2018, **140**, 3916–3928.

18 I. Monte Pérez, X. Engelmann, Y. M. Lee, M. Yoo, E. Kumaran, E. R. Farquhar, E. Bill, J. England, W. Nam and M. Swart, *Angew. Chem., Int. Ed.*, 2017, **56**, 14384–14388.

19 K. Ray, F. F. Pfaff, B. Wang and W. Nam, *J. Am. Chem. Soc.*, 2014, **136**, 13942–13958.

20 M. Guo, T. Corona, K. Ray and W. Nam, *ACS Cent. Sci.*, 2018, **5**, 13–28.

21 M. Maldonado-Domínguez and M. Srnec, *J. Am. Chem. Soc.*, 2020, **142**, 3947–3958.

22 X. Lu, X.-X. Li, Y.-M. Lee, Y. Jang, M. S. Seo, S. Hong, K.-B. Cho, S. Fukuzumi and W. Nam, *J. Am. Chem. Soc.*, 2020, **142**, 3891–3904.

23 S. Banerjee, A. Draksharapu, P. M. Crossland, R. Fan, Y. Guo, M. Swart and L. Que Jr, *J. Am. Chem. Soc.*, 2020, **142**, 4285–4297.

24 C. Colombari, E. V. Kudrik, P. Afanasiev and A. B. Sorokin, *J. Am. Chem. Soc.*, 2014, **136**, 11321–11330.

25 X. Engelmann, D. D. Malik, T. Corona, K. Warm, E. R. Farquhar, M. Swart, W. Nam and K. Ray, *Angew. Chem., Int. Ed.*, 2019, **58**, 4012–4016.

26 L. M. Dassama, A. Silakov, C. M. Krest, J. C. Calixto, C. Krebs, J. M. Bollinger Jr and M. T. Green, *J. Am. Chem. Soc.*, 2013, **135**, 16758–16761.

27 B. J. Wallar and J. D. Lipscomb, *Chem. Rev.*, 1996, **96**, 2625–2658.

28 M. Sono, M. P. Roach, E. D. Coulter and J. H. Dawson, *Chem. Rev.*, 1996, **96**, 2841–2888.

29 E. I. Solomon, T. C. Brunold, M. I. Davis, J. N. Kemsley, S.-K. Lee, N. Lehnert, F. Neese, A. J. Skulan, Y.-S. Yang and J. Zhou, *Chem. Rev.*, 2000, **100**, 235–350.

30 M. Costas, M. P. Mehn, M. P. Jensen and L. Que, *Chem. Rev.*, 2004, **104**, 939–986.

31 V. J. DeRose, K. E. Liu, S. J. Lippard and B. M. Hoffman, *J. Am. Chem. Soc.*, 1996, **118**, 121–134.

32 B. Singh, J. R. Long, F. Fabrizi De Biani, D. Gatteschi and P. Stavropoulos, *J. Am. Chem. Soc.*, 1997, **119**, 7030–7047.

33 V. V. Vu, T. M. Makris, J. D. Lipscomb and L. Que Jr, *J. Am. Chem. Soc.*, 2011, **133**, 6938–6941.

34 H. Nguyen, A. K. Shiemi, S. J. Jacobs, B. J. Hales, M. E. Lidstrom and S. I. Chan, *J. Biol. Chem.*, 1994, **269**, 14995–15005.

35 A. C. Rosenzweig, C. A. Frederick and S. J. Lippard, *Nature*, 1993, **366**, 537–543.

36 L. Que and W. B. Tolman, *Nature*, 2008, **455**, 333–340.

37 C. Krebs, D. Galonić Fujimori, C. T. Walsh and J. M. Bollinger, *Acc. Chem. Res.*, 2007, **40**, 484–492.

38 A. L. Feig and S. J. Lippard, *Chem. Rev.*, 1994, **94**, 759–805.

39 M. Merks and S. J. Lippard, *J. Biol. Chem.*, 2002, **277**, 5858–5865.

40 K. Yoshizawa and Y. Shiota, *J. Am. Chem. Soc.*, 2006, **128**, 9873–9881.

41 A. C. Rosenzweig, H. Brandstetter, D. A. Whittington, P. Nordlund, S. J. Lippard and C. A. Frederick, *Proteins: Struct., Funct., Genet.*, 1997, **29**, 141–152.

42 K. Kim and S. J. Lippard, *J. Am. Chem. Soc.*, 1996, **118**, 4914–4915.

43 A. M. Valentine, S. S. Stahl and S. J. Lippard, *J. Am. Chem. Soc.*, 1999, **121**, 3876–3887.

44 S.-K. Lee and J. D. Lipscomb, *Biochemistry*, 1999, **38**, 4423–4432.

45 T. C. Brunold, *Proc. Natl. Acad. Sci. U. S. A.*, 2007, **104**, 20641–20642.

46 P. E. Siegbahn and R. H. Crabtree, *J. Am. Chem. Soc.*, 1997, **119**, 3103–3113.

47 B. F. Gherman, B. D. Dunietz, D. A. Whittington, S. J. Lippard and R. A. Friesner, *J. Am. Chem. Soc.*, 2001, **123**, 3836–3837.

48 M. Costas, *Coord. Chem. Rev.*, 2011, **255**, 2912–2932.

49 W. Nam, *Acc. Chem. Res.*, 2007, **40**, 522–531.

50 S. P. de Visser, *J. Am. Chem. Soc.*, 2006, **128**, 9813–9824.

51 L. J. Murray and S. J. Lippard, *Acc. Chem. Res.*, 2007, **40**, 466–474.

52 C. E. Tinberg and S. J. Lippard, *Acc. Chem. Res.*, 2011, **44**, 280–288.

53 L. Shu, J. C. Nesheim, K. Kauffmann, E. Münck, J. D. Lipscomb and L. Que, *Science*, 1997, **275**, 515–518.

54 V. C.-C. Wang, S. Maji, P. P.-Y. Chen, H. K. Lee, S. S.-F. Yu and S. I. Chan, *Chem. Rev.*, 2017, **117**, 8574–8621.

55 E. C. Wilkinson, Y. Dong, Y. Zang, H. Fujii, R. Fraczkiewicz, G. Fraczkiewicz, R. S. Czernuszewicz and L. Que, *J. Am. Chem. Soc.*, 1998, **120**, 955–962.

56 M. H. Sazinsky and S. J. Lippard, *J. Am. Chem. Soc.*, 2005, **127**, 5814–5825.



57 S.-P. Huang, Y. Shiota and K. Yoshizawa, *Dalton Trans.*, 2013, **42**, 1011–1023.

58 B. Meunier, S. P. De Visser and S. Shaik, *Chem. Rev.*, 2004, **104**, 3947–3980.

59 S. Shaik, D. Kumar, S. P. de Visser, A. Altun and W. Thiel, *Chem. Rev.*, 2005, **105**, 2279–2328.

60 S. Shaik, S. Cohen, Y. Wang, H. Chen, D. Kumar and W. Thiel, *Chem. Rev.*, 2010, **110**, 949–1017.

61 A. B. Sorokin, E. V. Kudrik and D. Bouchu, *Chem. Commun.*, 2008, 2562–2564.

62 L. H. Do and S. J. Lippard, *J. Am. Chem. Soc.*, 2011, **133**, 10568–10581.

63 J. A. Broadwater, J. Ai, T. M. Loehr, J. Sanders-Loehr and B. G. Fox, *Biochemistry*, 1998, **37**, 14664–14671.

64 L. J. Murray, S. G. Naik, D. O. Ortillo, R. García-Serres, J. K. Lee, B. H. Huynh and S. J. Lippard, *J. Am. Chem. Soc.*, 2007, **129**, 14500–14510.

65 V. V. Vu, J. P. Emerson, M. Martinho, Y. S. Kim, E. Münck, M. H. Park and L. Que, *Proc. Natl. Acad. Sci. U. S. A.*, 2009, **106**, 14814–14819.

66 D. Usharani, D. Janardanan and S. Shaik, *J. Am. Chem. Soc.*, 2010, **133**, 176–179.

67 G. Xue, C. Geng, S. Ye, A. T. Fiedler, F. Neese and L. Que Jr, *Inorg. Chem.*, 2013, **52**, 3976–3984.

68 Y. Dong, H. Fujii, M. P. Hendrich, R. A. Leising, G. Pan, C. R. Randall, E. C. Wilkinson, Y. Zang and L. Que Jr, *J. Am. Chem. Soc.*, 1995, **117**, 2778–2792.

69 D. Wang, E. R. Farquhar, A. Stubna, E. Münck and L. Que, *Nat. Chem.*, 2009, **1**, 145–150.

70 E. V. Kudrik, P. Afanasiev, L. X. Alvarez, P. Dubourdeaux, M. Clémancey, J.-M. Latour, G. Blondin, D. Bouchu, F. Albrieux and S. E. Nefedov, *Nat. Chem.*, 2012, **4**, 1024–1029.

71 M. Ansari, N. Vyas, A. Ansari and G. Rajaraman, *Dalton Trans.*, 2015, **44**, 15232–15243.

72 M. G. Quesne, D. Senthilnathan, D. Singh, D. Kumar, P. Maldivi, A. B. Sorokin and S. P. de Visser, *ACS Catal.*, 2016, **6**, 2230–2243.

73 R. F. De Hont, G. Xue, M. P. Hendrich, L. Que Jr, E. L. Bominaar and E. Münck, *Inorg. Chem.*, 2010, **49**, 8310–8322.

74 H. Zheng, S. J. Yoo, E. Münck and L. Que, *J. Am. Chem. Soc.*, 2000, **122**, 3789–3790.

75 M.-H. Baik, M. Newcomb, R. A. Friesner and S. J. Lippard, *Chem. Rev.*, 2003, **103**, 2385–2420.

76 P. E. Siegbahn, *Inorg. Chem.*, 1999, **38**, 2880–2889.

77 P. Jayapal, A. Ansari and G. Rajaraman, *Inorg. Chem.*, 2015, **54**, 11077–11082.

78 M. J. Frisch, *et al.*, *GAUSSIAN 09 (Revision 02)*, Gaussian, Inc., Wallingford, CT, 2009.

79 S. Grimme, J. Antony, S. Ehrlich and H. Krieg, *J. Chem. Phys.*, 2010, **132**, 154104.

80 T. H. Dunning Jr and P. J. Hay, *Modern Theoretical Chemistry*, Plenum, New York, 1976, pp. 1–28.

81 P. J. Hay and W. R. Wadt, *J. Chem. Phys.*, 1985, **82**, 270–283.

82 W. R. Wadt and P. J. Hay, *J. Chem. Phys.*, 1985, **82**, 284–298.

83 R. Ditchfield, W. J. Hehre and J. A. Pople, *J. Chem. Phys.*, 1971, **54**, 724–728.

84 A. Schaefer, H. Horn and R. Ahlrichs, *J. Chem. Phys.*, 1992, **97**, 2571–2577.

85 C. Schaefer, C. Huber and R. Ahlrichs, *Chem. Phys.*, 1994, **100**, 5829–5835.

86 J. Tomasi, B. Mennucci and R. Cammi, *Chem. Rev.*, 2005, **105**, 2999–3094.

87 D. H. Ess and T. C. Cook, *J. Phys. Chem. A*, 2012, **116**, 4922–4929.

88 G. A. Zhurko, *ChemCraft software*, version 1.6, 2014.

89 S. Portmann and H. P. Luthi, *Chimia*, 2000, **54**, 766–770.

90 A. Ansari, M. Ansari, A. Singha and G. Rajaraman, *Chem.-Eur. J.*, 2017, **23**, 10110–10125.

91 C. Wang and H. Chen, *J. Am. Chem. Soc.*, 2017, **139**, 13038–13046.

92 K. Yoshizawa, *Acc. Chem. Res.*, 2006, **39**, 375–382.

93 P. Jayapal and G. Rajaraman, *Phys. Chem. Chem. Phys.*, 2012, **14**, 9050–9053.

94 D. E. Ferreira, W. B. De Almeida, A. Neves and W. R. Rocha, *Phys. Chem. Chem. Phys.*, 2008, **10**, 7039–7046.

95 R. Kumar, A. Ansari and G. Rajaraman, *Chem.-Eur. J.*, 2018, **24**, 6818–6827.

96 R. Kumar, B. Pandey and G. Rajaraman, *J. Indian Chem. Soc.*, 2019, **96**, 825–836.

97 B. Pandey, M. Jaccobab and G. Rajaraman, *Chem. Commun.*, 2017, **53**, 3193–3196.

98 B. Pinter, A. Chankisijjev, P. Geerlings, J. N. Harvey and F. De Proft, *Chem.-Eur. J.*, 2018, **24**, 5281–5292.

99 S. Essafi, D. P. Tew and J. N. Harvey, *Angew. Chem., Int. Ed.*, 2017, **56**, 5790–5794.

100 P. Rydberg, R. Lonsdale, J. N. Harvey, A. J. Mulholland and L. Olsen, *J. Mol. Graphics Modell.*, 2014, **52**, 30–35.

101 C. Wang, C. Zhao, L. Hu and H. Chen, *J. Phys. Chem. Lett.*, 2016, **7**, 4427–4432.

102 C. Zhao and H. Chen, *ACS Catal.*, 2017, **7**, 3521–3531.

103 J. Lu, B. Bi, W. Lai and H. Chen, *Angew. Chem., Int. Ed.*, 2019, **58**, 3795–3799.

104 Z. Tian, A. Fattah, L. Lis and S. R. Kass, *J. Am. Chem. Soc.*, 2006, **128**, 17087–17092.

105 Y.-R. Luo, *Comprehensive handbook of chemical bond energies*, CRC Press, 2007.

106 L. Noodleman, *J. Chem. Phys.*, 1981, **74**, 5737–5743.

107 T. Lovell, W.-G. Han, T. Liu and L. Noodleman, *J. Am. Chem. Soc.*, 2002, **124**, 5890–5894.

108 E. Ruiz, J. Cano, S. Alvarez and P. Alemany, *J. Comput. Chem.*, 1999, **20**, 1391–1400.

109 A. E. Reed, L. A. Curtiss and F. Weinhold, *Chem. Rev.*, 1988, **88**, 899–926.

110 W.-J. van Zeist and F. M. Bickelhaupt, *Org. Biomol. Chem.*, 2010, **8**, 3118–3127.

111 A. Diefenbach and F. M. Bickelhaupt, *J. Phys. Chem. A*, 2004, **108**, 8460–8466.

112 R. Strozier, P. Caramella and K. Houk, *J. Am. Chem. Soc.*, 1979, **101**, 1340–1343.

113 D. H. Ess and K. Houk, *J. Am. Chem. Soc.*, 2007, **129**, 10646–10647.



114 C. Y. Legault, Y. Garcia, C. A. Merlic and K. Houk, *J. Am. Chem. Soc.*, 2007, **129**, 12664–12665.

115 D. Usharani, D. C. Lacy, A. Borovik and S. Shaik, *J. Am. Chem. Soc.*, 2013, **135**, 17090–17104.

116 Note here that Ga<sup>III</sup> is a general dopant for Fe<sup>III</sup> and there are several experimental reports in the literature where Fe<sup>III</sup> is replaced by Ga<sup>III</sup>. (a) A. Cornia, M. Mannini, R. Sessoli and D. Gatteschi, *Eur. J. Inorg. Chem.*, 2019, 552–568; (b) P. King, T. C. Stamatatos, K. A. Abboud and G. Christou, *Angew. Chem., Int. Ed.*, 2006, **45**, 7379–7383.

117 E. J. Klinker, J. Kaizer, W. W. Brennessel, N. L. Woodrum, C. J. Cramer and L. Que Jr, *Angew. Chem., Int. Ed.*, 2005, **44**, 3690–3694.

118 Q. M. Phung, C. Martín-Fernández, J. N. Harvey and M. Feldt, *J. Chem. Theory Comput.*, 2019, **15**, 4297–4304.

119 M. J. Collins, K. Ray and L. Que, *Inorg. Chem.*, 2006, **45**, 8009–8011.

120 J. Kaizer, E. J. Klinker, N. Y. Oh, J.-U. Rohde, W. J. Song, A. Stubna, J. Kim, E. Münck, W. Nam and L. Que, *J. Am. Chem. Soc.*, 2004, **126**, 472–473.

121 J. Bautz, P. Comba, C. Lopez de Laorden, M. Menzel and G. Rajaraman, *Angew. Chem., Int. Ed.*, 2007, **46**, 8067–8070.

122 K. Benzing, P. Comba, B. Martin, B. Pokrandt and F. Keppler, *Chem.-Eur. J.*, 2017, **23**, 10465–10472.

123 P. Comba, S. Fukuzumi, C. Koke, B. Martin, A. M. Löhr and J. Straub, *Angew. Chem., Int. Ed.*, 2016, **55**, 11129–11133.

124 K. Anandababu, R. Ramasubramanian, H. Wadeppohl, P. Comba, N. Johnne Britto, M. Jaccob and R. Mayilmurugan, *Chem.-Eur. J.*, 2019, **25**, 9540–9547.

125 P. Comba, H. Rudolf and H. Wadeppohl, *Dalton Trans.*, 2015, **44**, 2724–2736.

126 C. V. Sastri, J. Lee, K. Oh, Y. J. Lee, J. Lee, T. A. Jackson, K. Ray, H. Hirao, W. Shin and J. A. Halfen, *Proc. Natl. Acad. Sci. U. S. A.*, 2007, **104**, 19181–19186.

127 P. Comba, D. Faltermeier, S. Krieg, B. Martin and G. Rajaraman, *Dalton Trans.*, 2020, **49**, 2888–2894.

128 S. A. Stoian, G. Xue, E. L. Bominaar, L. Que Jr and E. Münck, *J. Am. Chem. Soc.*, 2014, **136**, 1545–1558.

129 B. E. Sturgeon, D. Burdi, S. Chen, B.-H. Huynh, D. E. Edmondson, J. Stubbe and B. M. Hoffman, *J. Am. Chem. Soc.*, 1996, **118**, 7551–7557.

130 M. Feldt, Q. M. Phung, K. Pierloot, R. A. Mata and J. N. Harvey, *J. Chem. Theory Comput.*, 2019, **15**, 922–937.

131 Q. M. Phung and K. Pierloot, *Chem.-Eur. J.*, 2019, **25**, 12491–12496.

132 Q. M. Phung, M. Feldt, J. N. Harvey and K. Pierloot, *J. Chem. Theory Comput.*, 2018, **14**, 2446–2455.

133 A. Altun, M. Saitow, F. Neese and G. Bistoni, *J. Chem. Theory Comput.*, 2019, **15**, 1616–1632.

134 B. Mondal, F. Neese, E. Bill and S. Ye, *J. Am. Chem. Soc.*, 2018, **140**, 9531–9544.

135 Y. Guo, C. Riplinger, U. Becker, D. G. Liakos, Y. Minenkov, L. Cavallo and F. Neese, *J. Chem. Phys.*, 2018, **148**, 011101.

136 H. Chen, J. Song, W. Lai, W. Wu and S. Shaik, *J. Chem. Theory Comput.*, 2010, **6**, 940–953.

137 H. Chen, W. Lai and S. Shaik, *J. Phys. Chem. Lett.*, 2010, **1**, 1533–1540.

138 H. Chen, W. Lai, J. Yao and S. Shaik, *J. Chem. Theory Comput.*, 2011, **7**, 3049–3053.

139 S. Alvarez, P. Alemany, D. Casanova, J. Cirera, M. Llunell and D. Avnir, *Coord. Chem. Rev.*, 2005, **249**, 1693–1708.

140 W. Rasheed, A. Draksharapu, S. Banerjee, V. G. Young Jr, R. Fan, Y. Guo, M. Ozerov, J. Nehrkorn, J. Krzystek, J. Telser and L. Que Jr, *Angew. Chem., Int. Ed.*, 2018, **57**, 9387–9391.

141 S. Rana, J. P. Biswas, A. Sen, M. Clémancey, G. Blondin, J.-M. Latour, G. Rajaraman and D. Maiti, *Chem. Sci.*, 2018, **9**, 7843–7858.

142 K. B. Wiberg, *Tetrahedron*, 1968, **24**, 1083–1096.

143 J. Cano, E. Ruiz, S. Alvarez and M. Verdaguer, *Comments Inorg. Chem.*, 1998, **20**, 27–56.

144 M. Swart and M. Costas, *Spin states in biochemistry and inorganic chemistry: influence on structure and reactivity*, John Wiley & Sons, 2015.

145 E. Ruiz, S. Alvarez, A. Rodriguez-Forte, P. Alemany, Y. Pouillon and C. Massobiro, *Magnetism: Molecules to Materials*, ed. J. S. Miller and M. Drillon, Wiley-VCH, Weinheim, 2001.

146 H. Basch, K. Mogi, D. G. Musaev and K. Morokuma, *J. Am. Chem. Soc.*, 1999, **121**, 7249–7256.

147 D. Usharani, D. Janardanan, C. Li and S. Shaik, *Acc. Chem. Res.*, 2012, **46**, 471–482.

148 L. Bernasconi, M. J. Louwerse and E. J. Baerends, *Eur. J. Inorg. Chem.*, 2007, 3023–3033.

149 M. L. Neidig, A. Decker, O. W. Choroba, F. Huang, M. Kavana, G. R. Moran, J. B. Spencer and E. I. Solomon, *Proc. Natl. Acad. Sci. U. S. A.*, 2006, **103**, 12966–12973.

150 C. Geng, S. Ye and F. Neese, *Angew. Chem., Int. Ed.*, 2010, **49**, 5717–5720.

151 P. Barman, A. K. Vardhaman, B. Martin, S. J. Wörner, C. V. Sastri and P. Comba, *Angew. Chem., Int. Ed.*, 2015, **54**, 2095–2099.

152 S. Shaik, H. Chen and D. Janardanan, *Nat. Chem.*, 2011, **3**, 19–27.

153 H. Tang, J. Guan, H. Liu and X. Huang, *Dalton Trans.*, 2013, **42**, 10260–10270.

154 X. Sun, C. Geng, R. Huo, U. Ryde, Y. Bu and J. Li, *J. Phys. Chem. B*, 2014, **118**, 1493–1500.

155 M. Jaccob, A. Ansari, B. Pandey and G. Rajaraman, *Dalton Trans.*, 2013, **42**, 16518–16526.

156 D. Usharani, D. Janardanan, C. Li and S. Shaik, *Acc. Chem. Res.*, 2013, **46**, 471–482.

157 D. Janardanan, Y. Wang, P. Schyman, L. Que Jr and S. Shaik, *Angew. Chem., Int. Ed.*, 2010, **49**, 3342–3345.

158 M. Puri and L. Que Jr, *Acc. Chem. Res.*, 2015, **48**, 2443–2452.

159 J. F. Hull, D. Balcells, E. L. Sauer, C. Raynaud, G. W. Brudvig, R. H. Crabtree and O. Eisenstein, *J. Am. Chem. Soc.*, 2010, **132**, 7605–7616.

160 H. Tang, J. Guan, L. Zhang, H. Liu and X. Huang, *Phys. Chem. Chem. Phys.*, 2012, **14**, 12863–12874.

161 L. Ji, A. S. Faponle, M. G. Quesne, M. A. Sainna, J. Zhang, A. Franke, D. Kumar, R. van Eldik, W. Liu and S. P. de Visser, *Chem.-Eur. J.*, 2015, **21**, 9083–9092.



162 R. Hotzelmann, K. Wieghardt, U. Floerke, H. J. Haupt, D. C. Weatherburn, J. Bonvoisin, G. Blondin and J. J. Girerd, *J. Am. Chem. Soc.*, 1992, **114**, 1681–1696.

163 L. Bernasconi and E. J. Baerends, *J. Am. Chem. Soc.*, 2013, **135**, 8857–8867.

164 S. Shaik, D. Kumar and S. P. de Visser, *J. Am. Chem. Soc.*, 2008, **130**, 10128–10140.

165 D. Kumar, B. Karamzadeh, G. N. Sastry and S. P. de Visser, *J. Am. Chem. Soc.*, 2010, **132**, 7656–7667.

166 S. P. de Visser, *J. Am. Chem. Soc.*, 2010, **132**, 1087–1097.

167 D. Kumar, G. N. Sastry and S. P. De Visser, *Chem.-Eur. J.*, 2011, **17**, 6196–6205.

168 S. P. de Visser, D. Kumar, S. Cohen, R. Shacham and S. Shaik, *J. Am. Chem. Soc.*, 2004, **126**, 8362–8363.

169 T. H. Yosca, J. Rittle, C. M. Krest, E. L. Onderko, A. Silakov, J. C. Calixto, R. K. Behan and M. T. Green, *Science*, 2013, **342**, 825–829.

170 T. H. Yosca, A. P. Ledray, J. Ngo and M. T. Green, *J. Biol. Inorg. Chem.*, 2017, **22**, 209–220.

171 M. T. Green, *Curr. Opin. Chem. Biol.*, 2009, **13**, 84–88.

172 S. P. de Visser, *J. Am. Chem. Soc.*, 2009, **132**, 1087–1097.

173 S. Kumar, A. S. Faponle, P. Barman, A. K. Vardhaman, C. V. Sastri, D. Kumar and S. P. de Visser, *J. Am. Chem. Soc.*, 2014, **136**, 17102–17115.

174 D. Kumar, G. N. Sastry and S. P. De Visser, *Chem.-Eur. J.*, 2011, **17**, 6196–6205.

175 S. S. Shaik, *J. Am. Chem. Soc.*, 1981, **103**, 3692–3701.

